

A Tungsten Deep Neural-Network Potential for Simulating Mechanical Property Degradation Under Fusion Service Environment

Xiaoyang Wang

*Laboratory of Computational Physics,
Institute of Applied Physics and Computational Mathematics,
Huayuan Road 6, Beijing, P. R. China*

Yinan Wang

*School of Mathematical Sciences, Peking University,
No.5 Yiheyuan Road Haidian District, Beijing, P.R.China 100871*

Linfeng Zhang and Fuzhi Dai

*DP Technology, Beijing, 100080 and
AI for Science Institute, Beijing, 100084*

Han Wang*

*Laboratory of Computational Physics,
Institute of Applied Physics and Computational Mathematics,
Fenghao East Road 2, Beijing 100094, P.R. China and
HEDPS, CAPT, College of Engineering,
Peking University, Beijing 100871, P.R. China*

arXiv:2111.04281v3 [cond-mat.mtrl-sci] 20 Apr 2022

Abstract

Tungsten is a promising candidate material in fusion energy facilities. Molecular dynamics (MD) simulations reveal the atomistic scale mechanisms, so they are crucial for the understanding of the macroscopic property deterioration of tungsten under harsh and complex service environment. The interatomic potential used in the MD simulations is required to accurately describe a wide spectrum of relevant defect properties, which is by far challenging to the existing interatomic potentials. In this paper, we propose a new three-body embedding descriptor and hybridize it into the Deep-Potential (DP) framework, an end-to-end deep learning interatomic potential model. Trained with the dataset generated by a concurrent learning method, the potential model for tungsten, named by DP-HYB, is able to accurately predict a wide range of properties including elastic constants, stacking fault energy, the formation energies of free surfaces and point defects, which are included in the training dataset, and formation energies of grain boundaries and prismatic loops, the core structure of screw dislocation, the Peierls barrier and the transition path of the screw dislocation migration, which are not explicitly included in the training dataset. The DP-HYB is a good candidate for the atomistic simulations of tungsten property deterioration, especially those involving the mechanical property degradation under the harsh fusion service environment.

I. INTRODUCTION

Tungsten (W) and W alloys are refractory, high strength materials that are proved to be promising candidate structural materials in fusion devices of ITER project¹. Although W materials have multiple excellent properties such as high melting point, high thermal conductivity, high sputtering threshold and low atomic activity²⁻⁶, stable services under the extreme service environment in fusion devices are still challenging^{7,8}. During the services, the W materials are subject to mutual influences of high dose rate of neutron irradiation, plasma flushing and high heat load, etc.⁹, and the multi-physics coupling of these effects leads to severe deterioration of many properties critical to the stability of W materials. Among all the properties of W, the degradation of its thermal-mechanical properties are of the central concern. For example, irradiation induced defects act as obstacles to the gliding dislocations, and play major roles in the degradation of ductility¹⁰. The massive thermal load during W-plasma interaction leads to the formation of cracks beneath the W surface, and will degrade the mechanical strength¹¹. Besides, the high service temperature induces the coarsening of grains or even re-crystallization, which raises ductile-brittle transition temperature¹². All these processes under the service environments worsen the mechanical stability of the components in the fusion devices, thus increasing the risks to safety. To reveal how the processes occur requires the resolution of a series of critical atomistic events, which are not easily accessible to neither experimental approaches nor the continuum/meso scale simulations. Therefore, the large-scale atomistic simulation serves as an important tool to study the underlying nano-micro scale mechanisms responsible for the deterioration of the mechanical properties of W.

The potential energy surface (PES) is of central importance in atomistic simulations. To simulate property degradation under service conditions, the interatomic potential model is required to be applicable to a broad spectrum of properties. For example, a typical scenario under the multi-physics service condition is the poly-crystal W plastically deforming, driven by the external stress, while influenced by the irradiation induced damages. This case involves dislocation gliding, interaction with irradiation defects, pinning, de-pinning and interaction with grain boundaries. To conduct reliable atomistic simulation in this case, the requirement for the potential is the accurate evaluation of properties, including elastic

constants, dislocations, free surfaces, grain boundaries, point defects and their clusters by the same model.

The PES can be modeled from the quantum mechanical principles like the density functional theory (DFT), which has been proved to achieve relatively high accuracy and reliability. DFT has long been the *de facto* standard for calculating the properties like lattice parameters, cohesive energy, elastic constants and the formation energy of point defects. However, the computationally affordable sample size of DFT is usually limited to no more than 10^3 atoms due to the typical $\mathcal{O}(N^3)$ computational complexity (N being the number of atoms). For the macro-scale observable properties, such as yield strength, plasticity and work hardening, which are linked directly to extended defects, one needs to simulate systems composed of millions of atoms, a scale that goes far beyond the capability of typical DFT calculations. Thus, to simulate these properties, the development of a computationally affordable PES is in demand. The reliability of the interatomic potentials used in the complex service environment lies in two aspects¹³: (1) Good representability, i.e., the model can well reproduce all its training properties; (2) Good generalizability, i.e., the model is able to describe properties not explicitly presented in the training datasets. The generalizability can be classified as in-distribution and out-of-distribution generalizabilities, which describe the ability of the model to interpolate within and extrapolate out-of the distribution of training data, respectively. For example, trained with liquid configuration, the in-distribution generalizability means the ability of the model to accurately predict on other liquid configurations that are not in the training data, while the out-of-distribution generalizability means the ability of the model to predict on solid configurations.

The empirical or semi-empirical interatomic potential models the PES by a relatively simple analytical function form with tunable parameters, and is usually the method of choice in large scale atomistic simulation due to the $\mathcal{O}(N)$ computational complexity. Constant efforts have been made to develop reliable interatomic potentials from decades ago, and up to now dozens of potentials for W have been proposed. See, e.g., Refs.¹⁴⁻²⁴. Most of the potentials use fixed formalisms such as Finnis-Sinclair (FS)¹⁴, embedding atom method (EAM)¹⁵ and modified embedded atom method (MEAM)²⁵. The parameters of a potential are tuned by fitting the prediction of the potential to the DFT calculation or a group of experimentally measured properties. The two approaches can also be combined to tune the

potential model.

The analytical function forms of the empirical interatomic potential are usually developed based on physical and/or chemical knowledge, thus the empirical models may have a strong ability for generalization, in both senses of in-distribution and out-of-distribution. A good example is the Marinica-13 potential²¹, which is trained by 6 point defects, 2 perfect body centered cubic (BCC) and face centered cubic (FCC) and 10 liquid configurations, and is able to correctly predict many materials properties such as the formation energy of point defect clusters, the screw dislocation core-structure and a reasonably good Peierls barrier. The empirical interatomic potentials often suffer from representability issues, because the analytical function forms may not be flexible enough to fit a broad range of training targets. As a consequence, the empirical potentials are usually fitted to a relatively small collection of targets, and it is not trivial to increase the training dataset without loss of accuracy.

For the purpose of investigating the deterioration of the mechanical properties of W under service conditions, the state-of-the-art empirical potentials are not satisfactory. The Marinica-13²¹ potential predicts wrong relative stability of $\langle 111 \rangle$ and $\langle 100 \rangle$ prismatic loops (see Fig.3). Two later potentials, proposed by Bonny et. al.²⁶ and Setyawan et. al.²⁷, improved from the EAM-2 and EAM-4 of Marinica-13, respectively, still meet the same challenge (see Fig.3). The EAM potential proposed by Mason et. al.²⁸ is fitted to reproduce the interaction between vacancies in clusters and free surface formation energies, which have long been challenging for EAM potentials²⁹. This potential does not perform well when reproducing the generalized stacking fault energy (γ -line)³⁰. A more recent EAM potential proposed by Chen et. al.³¹ is fitted to lattice parameters, elastic constants and formation energy of point defects. It agrees well with its DFT database on these properties, and can be generalizable to other properties such as the generalized stacking fault energy (γ -line), but it gives a qualitatively wrong prediction on the screw dislocation core structure (the “Degenerate-core”, see the discussion in Sec. III F). Unfortunately, γ -line, screw dislocation core structure and dislocation loop formation energy are key tungsten properties under service environment. Thus even using these most advanced empirical potentials, the simulation results concerning the irradiation induced mechanical property changes will be in question.

Recent development of Machine-Learning(ML) potential^{24,32–41} hold the promise of having both the accuracy of DFT and efficiency of empirical potentials⁴². Previous successful

applications of Gaussian Approximation Potentials (GAP)⁴³ for W include two GAP potentials that considered different aspects of the properties. The GAP potential proposed by Szlachta, Bartók and Csányi⁴⁴ (GAP-1) considered properties of bulk, elastic, mono-vacancy, free surfaces, stacking fault energy and screw dislocation and excluded the self-interstitial atoms (SIA), while the GAP potential proposed by Byggmästar et. al.⁴⁵ (GAP-2) additionally included SIAs, their clusters, vacancy clusters, short-range repulsion, liquid phase, distorted surfaces in the training dataset, but omitted the stacking fault energy and screw dislocation properties. The computational cost of the GAP potentials is in proportional to the size of their training dataset, thus it is not common to include all relevant configurations in the training dataset for the sake of efficiency, and a balance between the accuracy and efficiency is carefully searched⁴⁴. This feature of GAP potentials makes it too expensive to take advantage of large databases, which further limits the ability of generalization to properties dissimilar to what are included in its training datasets. For example, the accuracy of GAP-2 on large SIA clusters would not be satisfactory until including di-SIA cluster configurations in the training dataset⁴⁵, and without the explicit consideration of dislocation properties, the GAP-2 presents an obviously lower Peierls barrier than DFT⁴⁶. Thus, none of the GAP models can be directly used to conduct atomistic simulation on mechanical property degradation of W. A more efficient implementation of ML potential on W is the spectral neighbor analysis potential (SNAP)²⁴. In this potential a subset of GAP-1 training database is utilized. In addition, it included the configurations of equation of states, liquid phases and multiple vacancies in its training dataset. Meanwhile, it omitted the screw dislocation structures and generalized stacking fault. Thus extended defect properties such as generalized stacking fault energy and Peierls stress are overestimated by the SNAP⁴⁷ potential. During the preparation of this manuscript, we noticed the publication of a new formalism of ML potential, namely, the quadratic-noise ML potential⁴⁸ for the crystal defect of W. This ML potentials takes a simpler form and targets mainly the properties of point-defect clusters and dislocations. Although the robustness of generalization outperforms the GAP models due to its preconditioned linear-ML fitting, its representability is expected to be lower than the GAP formalism.

Benefited from the excellent ability of neural-networks to fit to high-dimensional, multi-variant functions, the deep-neural-network (DNN) based interatomic potentials have shown

a great capability of describing multi-component materials' properties^{13,49–59}. In addition, the computational cost of DNN is determined by the size of neural-network and the size of the system, and is independent on the size of training datasets. This feature of DNN makes it practical to take advantage of relatively large datasets. Although the extensible and symmetries are strictly satisfied by the DNN potential models, the generalizability of them are often put in question. A well-known fact is that the out-of-distribution generalizability of DNNs is not expected⁶⁰. The questions faced by DNN based potential models come to (1) how to generate a training dataset that covers the relevant configuration space as comprehensively as possible, and (2) how well can the model generalize in the sense of in-distribution, so all the desired properties can be reproduced at the DFT accuracy. Since the out-of-distribution generalizability of DNNs should be entirely forgotten, in the rest of the paper, when we refer to the word “generalizability”, we mean the in-distribution generalizability.

In this paper, we use the Deep-Potential (DP) method to establish a highly generalizable interatomic potential for BCC W. This potential is highlighted by adopting our newly-designed symmetry-preserving descriptor, namely, three-body embedding, which, in addition to the bond-angle contributions encoded in the environment matrix, explicitly considers the bond-angle contributions in the embedding part of the descriptor⁴¹. The formalism of the new descriptor is inspired by the nature of BCC transition metals²¹: their d-bands are not fully filled, which leads to a relatively complex shape of the electron density distribution with obvious angular characters⁶¹. Thus, explicitly considering these bond-angle embedding is expected to increase the representability of the model to transition metals such as W. Trained with the large dataset automatically generated by the concurrent learning strategy Deep-Potential GENerator (DP-GEN)⁶², the W DP model is proved to be in satisfactory agreement with DFT and/or experiment in a wide range of properties including bulk properties, elastic constants, formation energies of surfaces/interfaces, point defects and their clusters as well as the major aspects of screw dislocation properties such as the core structure, the Peierls barrier and the dislocation trajectory during its migration. A majority of the investigated properties, i.e., the formation energy of prismatic loops and C15 Laves phase clusters, interaction energy between neighboring vacancies, screw dislocation core structures and migration path, Peierls barrier and grain boundary structures, are blind to the DP

model in the sense that the corresponding configurations are not explicitly included in the training dataset. Thus, we argue that the DP model is of high generalizability. Moreover, due to the high representability of DP models, this W DP potential can be feasibly adjusted to describe more properties of interest according to the purpose of different simulations.

The manuscript is organized as follows. In Section II, we introduce the mathematical structure of the DP descriptor and the three-body embedding descriptor. Then we describe the details of the concurrent learning scheme. In Section III, we present the benchmark results of DP models on properties of W, and make comparisons with results obtained by DFT calculations and by a wide range of previous empirical/ML potentials. Then we draw conclusive remarks in Section IV.

II. METHOD

A. The Deep Potential Model

The DP model assumes that the potential energy of the system can be decomposed into atomic contributions $E = \sum_i E_i$, where E and E_i denote the system energy and the contribution due to atom i , respectively. The atomic energy E_i depends on the position of atom i , and its near neighbors, whose distances to i are less than the cutoff radius. We denote the positions of atoms in the system by $\{\mathbf{r}_1, \dots, \mathbf{r}_N\}$, and define the *environment matrix* for i , which records all the relative positions of near neighbors to i , by

$$(\mathcal{R}_i)_{j,\cdot} = s(r_{ij}) \times \left(\frac{x_{ij}}{r_{ij}}, \frac{y_{ij}}{r_{ij}}, \frac{z_{ij}}{r_{ij}} \right), \quad (1)$$

where $r_{ij} = |\mathbf{r}_{ij}|$, $\mathbf{r}_{ij} = \mathbf{r}_j - \mathbf{r}_i$, (x_{ij}, y_{ij}, z_{ij}) are the three Cartesian components of \mathbf{r}_{ij} . $s(r_{ij}) = f_c(r_{ij})/r_{ij}$ with f_c being a switching function smoothly varies from 1 to 0 at the cutoff distance. The environment matrix has N_m rows, where N_m is the maximally possible number of neighbors, and Eq. (1) presents the definition of the j -th row. When the real number of neighbors, denoted by $N(i)$ is less than N_m , the environment matrix is padded with zeros. The DP models the atomic energy contribution E_i by

$$E_i = \mathcal{F}\left(\mathcal{D}(\mathcal{R}_i)\right), \quad (2)$$

where \mathcal{D} is the descriptor that maps the environment matrix to symmetry preserving features, and \mathcal{F} is the fitting net that represents the energy dependency on the local atomic configuration. It is noted that the descriptor can be hybridized with several descriptors, i.e. the concatenation of symmetry preserving features with different designs,

$$\mathcal{D} = \left(\mathcal{D}^{(2)}, \mathcal{D}^{(3)}, \dots \right). \quad (3)$$

The smooth edition of the DP⁴¹ proposes the following descriptor

$$\mathcal{D}_i^{(2)} = \frac{1}{N_m^2} (\mathcal{G}_i^{(2),<})^T \tilde{\mathcal{R}}_i (\tilde{\mathcal{R}}_i)^T \mathcal{G}_i^{(2)} \quad (4)$$

where $\tilde{\mathcal{R}}_i$ is the *generalized environment matrix* defined by

$$(\tilde{\mathcal{R}}_i)_j = s(r_{i,j}) \times \left(1, \frac{x_{ij}}{r_{ij}}, \frac{y_{ij}}{r_{ij}}, \frac{z_{ij}}{r_{ij}} \right), \quad (5)$$

and $\mathcal{G}_i^{(2)}$ is the *embedding matrix* involving two-atom distance and is defined as

$$(\mathcal{G}_i^{(2)})_{j,\cdot} = \left(G_1^{(2)}(s(r_{ij})), \dots, G_{M_2}^{(2)}(s(r_{ij})) \right), \quad (6)$$

where $G^{(2)}$ is the two-body embedding network, represented by a DNN mapping from a single value $s(r_{ij})$, through multiple hidden layers, to M_2 outputs (also the number of columns of $\mathcal{G}_i^{(2)}$). The Eq. (6) defines the j -th row of the embedding matrix. The embedding matrix in total has N_m rows and is pad with zeros if $N(i) < N_m$. The $\mathcal{G}_i^{(2),<}$ denotes a sub-matrix of $\mathcal{G}_i^{(2)}$ containing the first $M^<$ columns of $\mathcal{G}_i^{(2)}$. We refer the embedding matrix defined by Eq. (6) as the *two-body embedding matrix*, because it only involves distances between two atoms, i.e. r_{ij} , in the construction. More mathematical details regarding the two-body embedding network and embedding matrix are found in the Supplementary Material Sects. IIA and IIB.

In most cases, the two-body descriptor is expressive enough to achieve a satisfactory accuracy, even in the most stringent test of the accuracy of potential energy such as the phase diagram of water⁵⁰. However, as a typical BCC transition metal, W has unfilled d -bands thus has more complex shape of electronic density distribution. In these metals, the bond-angle contribution are essential to the proper description of materials properties⁶¹. This makes the bond-angle contribution in W playing significant roles in the prediction of potential energy²¹. Though in the descriptor of the smooth edition of DP (4), the bond-angle contribution has been considered by the multiplication of the generalized environment matrices $\tilde{\mathcal{R}}_i (\tilde{\mathcal{R}}_i)^T$,

further incorporating the bond-angle contribution explicitly into the embedding matrix is expected to increase the representability for BCC transition metals.

This inspires us to propose the following *three-body embedding tensor*

$$(\mathcal{G}_i^{(3)})_{jk,\cdot} = \left(G_1^{(3)}((\theta_i)_{jk}), \dots, G_{M_3}^{(3)}((\theta_i)_{jk}) \right), \quad (7)$$

which is an order 3 tensor with the first two indices running over all neighbors and the third one goes from 1 to M_3 . The vector $G^{(3)}$ of length M_3 is represented by a DNN and is trainable. In Eq. (7),

$$(\theta_i)_{jk} \equiv (\mathcal{R}_i)_{j,\cdot} \cdot (\mathcal{R}_i)_{k,\cdot} = s(r_{ij})s(r_{ik}) \frac{\mathbf{r}_{ij} \cdot \mathbf{r}_{ik}}{r_{ij}r_{ik}}, \quad (8)$$

is the dot product of row j and row k of the environment matrix \mathcal{R}_i , and encodes the bond-angle information of the two neighbors j and k of atom i . We thus define a new descriptor $\mathcal{D}_i^{(3)}$ from the three-body embedding tensor as

$$\mathcal{D}_i^{(3)} = \frac{1}{N_m^2} \theta_i : \mathcal{G}_i^{(3)} = \frac{1}{N_m^2} \sum_{jk=1}^{N_m} (\theta_i)_{jk} (\mathcal{G}_i^{(3)})_{jk}, \quad (9)$$

where $:$ denote the double summation over the j and k indices of the matrix θ_i (defined by Eq. (8)) and the three-body embedding tensor $\mathcal{G}_i^{(3)}$. It is straightforward to prove that the descriptor Eq. (9) is invariant under translational, rotational and permutational transforms. In the Supplementary Materials Sects. IIC and IID, we provide all detailed information of the mathematical formula of the three-body embedding tensor and descriptor, and provide the proof of the symmetries of the descriptor.

The computational cost of the descriptor $\mathcal{D}^{(2)}$ is proportional to the number of neighbors in the neighbor list, while the complexity of the $\mathcal{D}^{(3)}$ is in proportional to the square of the number of neighbors. On the other hand, the precise description of the neighbor angles are only critical for the neighboring atoms within the first few neighbor shells⁴⁰, and for the neighbors far away embedding the distance is enough for describing the local configuration. Therefore, we adopt a relatively small cutoff radius for the three-body embedding (4 Å) while a relatively large cutoff (6 Å) for the two-body embedding, then hybridize the two descriptors as $\mathcal{D} = (\mathcal{D}^{(2)}, \mathcal{D}^{(3)})$. In this work we refer to the DP using this hybridized descriptor as DP-HYB. The newly proposed DP approach is extensively compared with the smooth edition of DP (denoted by DP-SE2) that uses the descriptor $\mathcal{D} = \mathcal{D}^{(2)}$.

B. DP-GEN Scheme

We use the concurrent learning strategy named DP-GEN^{13,62} to generate the optimal training dataset in the sense that it is the most compact and adequate dataset to guarantee a uniform accuracy of DP in the relevant configuration space. DP-GEN is a close-loop iterative workflow, including exploration, labeling and training steps. Starting from an initial dataset, an ensemble of DP models is trained. Then one of the models is used to explore the configuration space by simulation techniques like molecular dynamics (MD), Monte Carlo (MC), structure optimization or enhanced sampling. The DP prediction error on the explored configurations is estimated by the deviation of the predictions of the ensemble of DP models, and only a small subset of the configurations with large errors are selected for labeling, i.e. for the DFT calculations of energy, forces and virial tensor. The iteration is converged when the prediction error on all explored configurations are tolerable. The DP-GEN scheme has successful applications in the Al-Mg binary¹³ and Al-Mg-Cu ternary alloys⁴⁹, water in a very large thermodynamic region⁵⁰, Ag-Au nanoalloys⁵¹, etc.

a. Initial dataset. The initial dataset is composed of three parts:

1. The equilibrated unit cells of the BCC, the FCC, the hexagonal close-packed (HCP) and diamond structures.
2. Artificially strained and perturbed structures. Hydrostatic strain is applied to equilibrated structures by changing lattice parameters ranging from 96% to 106% at a step 2%. Perturbations are then exerted on each structure under strain. The atom positions are randomly perturbed with a maximal displacement of 0.01 Å. The cell is randomly perturbed by 3%.
3. AIMD trajectory of the deformed structures. Setting each compressed structure under perturbation as initial configuration, AIMD simulations are conducted with 5 steps under temperature 100K.

All the data are labeled with DFT calculations (see part *c. Labeling* for more details). In other words, the DFT-calculated energy, atomic forces and virial tensor of each structure are recorded.

b. Exploration. The LAMMPS package⁶³ compiled with the DeePMD-kit⁶⁴ support is employed to perform Deep Potential molecular dynamics (DPMD)⁴⁰ simulations for the exploration of the configuration space. The exploration uses 4 subsets of configurations as the initial configurations for the MD sampling. The initial configurations, simulation ensemble, temperatures and pressures conditions are summarized in the following and in the Table I.

1. The strained and perturbed $2 \times 2 \times 2$ supercell BCC W bulk. NPT ensemble. Temperature 50 to 5100 K. Pressure -2 to 5 GPa.
2. The strained and perturbed $3 \times 3 \times 3$ supercell BCC W bulk. NPT ensemble. Temperature 50 to 5100 K. Pressure -2 to 5 GPa.
3. (111),(110) and (112) free surfaces. NVT ensemble. Temperature 300 to 1800K.
4. Locally perturbed $2 \times 2 \times 2$ and $3 \times 3 \times 3$ supercells of BCC W bulk. NVE ensemble.

During the exploration, the deviation of force predictions of four DP models, trained with identical hyper-parameters but different random seeds, is used to estimate the error in the force prediction. If the maximal deviation of atomic forces is higher than $0.20 \text{ eV}/\text{\AA}$ but lower than $0.35 \text{ eV}/\text{\AA}$, the configuration is considered as a candidate configuration and sent for labeling.

c. Labeling. The labels of the candidate configurations, i.e. the energy, force, and virial tensor, are computed by DFT with exchange-correlation modeled by the generalized gradient approximation (GGA) proposed by Perdew, Burke and Ernzerhof (PBE)⁶⁵. The DFT calculations were conducted using VASP^{66,67} package. The Brillouin zone is sampled by the Monkhorst-Pack method with a grid spacing of 0.16\AA^{-1} . The projector-augmented-wave (PAW) method is used and the energy cut-off of the plane-wave basis set is set to 600 eV. The 6s and 5d electrons are considered valence electrons. The convergence criterion for the self-consistent field iteration is set to 10^{-6} eV. The same DFT parameters are also used for labeling the initial dataset.

d. Training. In each iteration, four models are trained simultaneously using the same dataset and hyper-parameters, with the only difference being the random seeds employed to initialize the model parameters. The sizes of the hidden layers of the two-body embedding nets $G^{(2)}$ are (20, 40, 80), while the three-body embedding $G^{(3)}$ has hidden layers of sizes

(4, 8, 16). The hidden layers of the fitting nets are set to (240, 240, 240). The Adam stochastic gradient descent method⁶⁸ with the default hyper-parameter settings provided by the TensorFlow package⁶⁹ is used to train the DP models. The learning rate is exponentially decayed with starting and final learning rates set to 1×10^{-3} and 5×10^{-8} , respectively. In each DP-GEN iteration the DP model is trained with 4×10^5 steps. After the DP-GEN iterations converge, the productive models are trained with 2.4×10^7 steps. The size of the DNNs used in the DP models, and other hyper-parameters are provided in the Supplementary Material Table SI.

e. Refinement. The productive DP models are firstly refined with DFT labeled structures of SIA structures, the γ -line and (100) surface structure. SIA data is generated via additional DP-GEN iterations, with three types of SIA structures (namely $\langle 111 \rangle$, $\langle 110 \rangle$ and $\langle 100 \rangle$ dumbbells) as initial configurations, the explored temperature ranges from 50K to 600K. γ -line structures are obtained directly from the DFT γ -line calculation along $\langle 111 \rangle$ directions on $\{110\}$ and $\{112\}$ planes. We also included relaxed and unrelaxed (100) free surface data in the refining dataset. The refined models are trained for 1×10^6 steps with model parameters initialized by the productive model. The starting learning rate is set to 1×10^{-4} , and the starting prefactors of energy, force and virial tensors, p_ϵ^{start} , p_f^{start} , p_ξ^{start} are set to 1.0, 1.0 and 0.9, respectively (See the Supplementary Material for the definition of the prefactors). The other hyper-parameters are the same as those used to train the productive model. Then, the DP models are further refined by the isolated W atom energy. All the hyper-parameters are the same with those used in the first refinement except that the number of training steps is set to 4×10^6 . The energy of an isolated atom is calculated with spin-polarized DFT. Benchmark results are based on the model after the refinements.

The composition of the training dataset is provided in Table I. The training database consists of a total number of 43,648 configurations (1,103,542 local atomistic environments). The root mean square error (RMSE) of the energy (normalized by the number of atoms), the atomic forces, and the virial tensor (normalized by number of atoms) on the entire training dataset are 6.958×10^{-3} eV/atom, 1.278×10^{-1} eV/Å and 1.186×10^{-1} eV/atom, respectively. The training error on each subset of the training dataset is shown in Table I.

TABLE I: The components of the training dataset. The initial dataset, and the sub-datasets generated by DP-GEN MD explorations starting from different initial configurations under various thermodynamic conditions are summarized. The bulk samples are heated up to 5100K to guarantee the coverage of liquid structures. We also list the number of configurations (n_{conf}), number of the local atomistic environments (n_{env}) and training errors of energies and forces in the sense of RMSE of each sub-dataset.

Initial confs./Initial data	Ensemble	n_{conf}	n_{env}	RMSE $_E$ (eV/Atom)	RMSE $_F$ (eV/Å)
Initial dataset	-	7060	17720	4.815×10^{-3}	7.711×10^{-2}
2x2x2 Bulk BCC W	NPT 50-5100K -2 to 5Gpa	4379	70064	1.186×10^{-2}	2.478×10^{-1}
3x3x3 Bulk BCC W	NPT 50-5100K -2 to 5Gpa	2395	129330	7.508×10^{-3}	2.601×10^{-1}
(110),(112) Free Surface	NVT 300-1800K	5477	49770	1.210×10^{-2}	1.575×10^{-1}
(111) Free Surface	NVT 300-1800K	1536	146240	1.711×10^{-3}	1.136×10^{-2}
Local Perturbation	NVE	19943	500120	4.295×10^{-3}	8.676×10^{-2}
Refine Dataset	Ensemble	n_{conf}	n_{env}	RMSE $_E$ (eV/Atom)	RMSE $_F$ (eV/Å)
(100) Free Surface	NVT 300-1800K	1315	52600	2.290×10^{-3}	1.180×10^{-1}
Generalized Stacking Fault	-	286	4752	8.564×10^{-3}	5.690×10^{-2}
Point defects	NVT 50-600K	1257	132946	3.980×10^{-4}	3.348×10^{-2}
Isolated Atom	-	1	1	7.004×10^{-3}	0

III. VALIDATION OF THE DEEP POTENTIALS

In this section, benchmark results of DP models of W are presented. The presented results include bulk properties, formation energies of point defects and prismatic loops, screw dislocation properties, generalized stacking fault energies, formation energies of free surfaces and typical grain boundaries. These properties are critical to the mechanical properties of W under service environment. Our goal is to test if the W DP-HYB and DP-SE2 models are able to accurately predict all these properties. Comparisons are made among the DP-HYB, DP-SE2, DFT and other interatomic potentials including the empirical and machine learning potential models.

Due to the large amount of empirical interatomic potentials reported in literature, it is impossible to comprehensively test all of them, so we only consider a limited subset, i.e. the potentials by Ackland and Thetford et. al. (AT)⁷⁰, Juslin and Wirth (JW)²³, Mason et. al. (MN)²⁸, Chen and Li et. al. (CL)³¹. Two EAM potentials, MV-2-B by Bonny et. al.²⁶ and MV-4-S by Setyawan et. al.²⁷, modified from the potentials MV-2 and MV-4 developed by Marinica et. al.²¹, are also considered. For AT, JW and MN, we mainly take the reference

values from previous literature^{23,28,70}, and for CL, MV-2-B and MV-4-S we reproduce the properties by ourselves for comparison. Two GAP machine learning potentials are also included for comparisons, i.e. the GAP model by Csanyi et. al. (GAP-1)⁴⁴, and by Byggmästa et. al. (GAP-2)⁴⁵. GAP-1 was publicly available, but is currently not available from the broken (<http://www.libatoms.org/> accessed on Mar.30 2022) and redirected (<https://libatoms.github.io/GAP/> accessed on Mar.30 2022) web-links. Thus we mainly take the presented results from the paper of GAP-1⁴⁴. For GAP-2, we take the presented results from Ref.⁴⁵ and calculate the un-presented properties using the published GAP-2 potential.

A. Bulk Properties

The lattice parameter (a_0), cohesive energy of BCC/FCC lattices ($E_{\text{BCC}}, E_{\text{FCC}}$) and three independent elastic constants (C_{11} , C_{12} and C_{44}) of BCC W are reported in Table II. DP predicted results are compared with our DFT calculations, while the EAM potentials and the GAP potentials are compared with the corresponding fitting targets.

Accurate prediction of these ground-state properties is the basis of evaluating all other surface and defect properties. The W DP models have satisfactory agreement with our DFT calculation on the predictions of lattice parameters, cohesive energies and elastic constants, since these properties are well-presented in the initial training dataset. The DP-HYB model has a slightly higher accuracy than DP-SE2 model on cohesive energies due to the improved representability. The ground-state properties are the fitting targets of the investigated empirical potentials, and all the potentials can accurately reproduce the values in the training datasets. When comparing across different EAM potentials, they show notable differences in the lattice parameters, because they are fitted to different target values. For example, CL potential was fitted to the experimental value 3.165 Å, MV-2-B and MV-4-S agree with the DFT calculation that gave 3.14 Å⁷¹. However, due to the strict requirement of self-consistence in training dataset, DP-SE2 and DP-HYB models are fitted only to our DFT data, which are, like other DFT results^{45,71,72}, slightly different from the experimental values. Likewise, as the BCC crystal of W is sampled in a wide range of stress during the DP-GEN iterations, the elastic constants of both DP models are in good agreement with the DFT, which gives a higher C_{11} and lower C_{44} than experimental results⁷³ due to the

TABLE II: Lattice parameters, cohesive energies and elastic constants predicted by EAM, GAP and DP models and our DFT calculation. The experimental values are provided in parenthesis. $a_{0,\text{BCC}}$ and $a_{0,\text{FCC}}$ denote the lattice parameters of BCC and FCC W at zero temperature, respectively. E_{BCC} and E_{FCC} denote the BCC and FCC lattice cohesive energies. C_{11}, C_{12}, C_{44} are independent elastic constant components of the BCC crystal. AT, JW and MN are fitted to experimental data. The CL and MV EAM potentials and the machine learning potentials are compared with their fitting targets. The * in the table indicates that the property is included in the training data as a fitting target, but the value is not presented in the reference.

Potential	$a_{0,\text{BCC}}(\text{\AA})$	$E_{\text{BCC}}(\text{eV})$	$C_{11}(\text{GPa})$	$C_{12}(\text{GPa})$	$C_{44}(\text{GPa})$	$a_{0,\text{FCC}}(\text{\AA})$	$E_{\text{FCC}}(\text{eV})$
MV-2-B ²⁶	3.14	-8.9	522	203	160	3.793	-8.53
MV-4-S ²⁷	3.143	-8.9	522	202	161	3.738	-8.62
MV fitting target ²¹	(3.165) ⁷⁵	-8.9 ⁷⁵	523 ⁷⁵	203 ⁷⁵	160 ⁷⁵	4.054 ⁷⁶	-8.43 ⁷⁶
AT ⁷⁰	3.165	-8.9	522	204	161	3.927	-8.75
JW ²³	3.165	-8.9	522	204	161	3.927	-8.75
MN ²⁸	3.164	-8.9	526	204	161	3.927	-8.75
Experimental	(3.165) ⁷⁷	(-8.9) ⁷⁷	(522) ⁷³	(204) ⁷³	(161) ⁷³	-	-
CL ³¹	3.165	-8.9	523	204	161	4.103	-8.62
CL fitting target ³¹	3.165	-8.9	523	204	161	4.00	-8.33
GAP-1 ⁴⁴	3.181	-	518	198	143	-	-
GAP-1 fitting target ⁴⁴	3.181	-	517	198	142	-	-
GAP-2 ⁴⁵	3.185	-8.39	526	200	149	*	*
GAP-2 fitting target ⁴⁵	3.185	-8.39	522	195	148	*	*
DP-SE2	3.172	-8.46	526	192	138	4.023	-7.96
DP-HYB	3.172	-8.47	543	203	141	4.023	-7.97
DFT (this work)	3.171	-8.47	548	200	147	4.023	-7.98

pseudopotential used in the calculation⁷⁴.

The equations of states (EOS) of BCC W predicted by the DP models are shown in

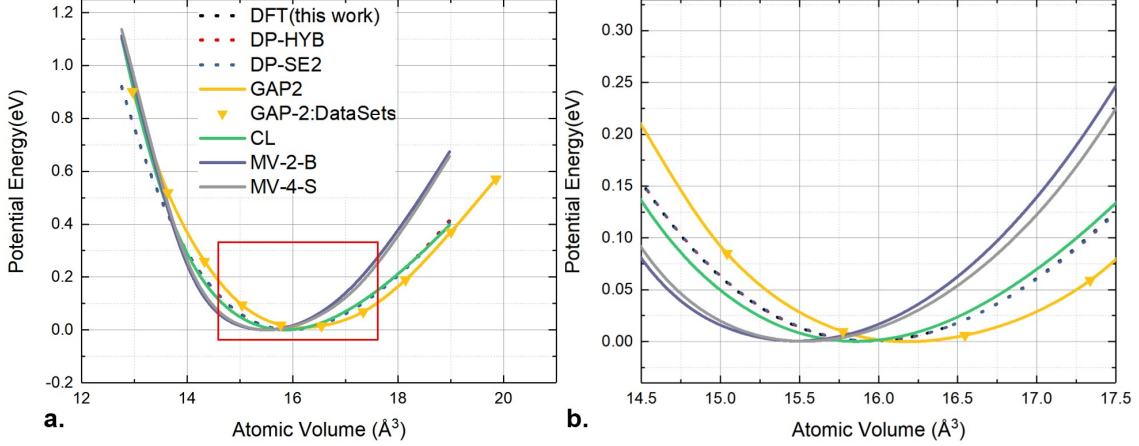


FIG. 1: EOSs of BCC W predicted by DFT, DP models and three previous EAM models. All the curves are shifted by the energy of the stable BCC structure. a) EOS curve in atomic volume ranging from 12 \AA^3 to 19 \AA^3 . b) Enlarged figure near bottom of the EOS curves.

Fig. 1. We calculated the EOSs of EAM potentials CL, MV-2-B, MV-4-S, and take the EOS calculation result of GAP-2 from Ref.⁴⁵. All EOSs are shifted by their corresponding ground-state energies of the BCC W. Both DP-SE2 and DP-HYB are in almost perfect agreement with our DFT calculation. The main difference between the EOSs calculated by the EAM and DP models are attributed to the different predictions of the lattice parameter. As the system is compressed (volume smaller than the equilibrium volume), the increment of energy of all EAM potentials is faster than the DFT calculation. A faster increment of energy of MV-2-B and MV-4-S is also observed as the system is expanded (larger volume side). GAP-2 exhibits a similar tendency of change of EOS against volume with both DP and DFT results. GAP-2 predicts the minimum EOS at around 16.2 \AA^3 , slightly larger than the results predicted by DP models, due to the different pseudopotential used when constructing the database⁴⁵.

Both the DP-SE2 and DP-HYB models show good agreements with DFT calculation on the basic bulk properties of BCC W. Many other defect structure properties depend on these basic properties. To further validate the representability and generalizability of W DP models, in the following subsections the surface and defective structure properties are investigated.

TABLE III: Formation energies of free surfaces with different miller indices are calculated using DP models and DFT, and previous results using EAM and GAP models are also presented for comparison. The EAM potentials AT, JW, MV-2-B, MV-4-S and CL are not fitting against the surface formation energies. The EAM potential MN, machine learning potentials GAP-1, GAP-2, DP-SE2 and DP-HYB have surface training data. Their fitting targets are presented along with the corresponding models. Data in the parenthesis is the unrelaxed surface energy. The units of free surface formation energy is: J/m^2 .

Potential	(111)	(122)	(110)	(112)	(120)	(100)
AT ⁷⁰	3.300	-	2.571	3.045	-	2.923
JW ²³	3.300	-	2.575	3.045	-	2.923
MV-2-B ²⁶	2.963	-	2.306	2.752	-	2.723
MV-4-S ²⁷	3.217	-	2.508	2.99	-	2.93
CL ³¹	3.263	-	2.541	2.989	-	2.893
MN ²⁸	4.155	-	3.497	3.866	-	3.841
Fitting Target of MN	4.453	-	4.005	4.181	-	4.646
GAP-1 ⁴⁴	3.557	-	3.268	3.461	-	4.037
GAP-2 ⁴⁵	3.525	3.589	3.348	3.428	3.781	4.021
Fitting Target of GAP	3.556	-	3.268	3.460	-	4.021
DP-SE2	3.543	3.682	3.366	3.420	3.581	3.937
	(4.040)	(4.050)	(3.418)	(3.720)	(3.874)	(4.295)
DP-HYB	3.540	3.625	3.333	3.433	3.647	3.923
	(4.051)	(4.002)	(3.402)	(3.759)	(3.899)	(4.308)
DFT (this work)	3.534	3.618	3.315	3.453	3.689	4.048
	(4.053)	(3.941)	(3.380)	(3.797)	(4.005)	(4.342)

B. Free Surfaces

The formation energies of free surfaces with different miller indices are calculated using the DP models and DFT, and are shown in Table. III. The DP models predict that the

surface with the lowest formation energy is (110), in agreement with the DFT calculation and the reference. The DP models achieve high accuracy in the (111), (110), (112) and (100) surfaces. Noticing that these surface structures present in the training dataset, the high accuracy indicates good representability of the DP models. Meanwhile, the DP models are accurate in describing the (122) and (120) surfaces, whose structures are not explicitly included in the training data. Noticing that these surfaces can decompose into the free surfaces in the training dataset, thus the accuracy is a consequence of generalization (in the sense of in-distribution). Moreover, the DP models are able to correctly describe the un-relaxed free surfaces (presented in parentheses in Table. III) of the investigated miller indices. The accurate evaluation of free-surface formation energy can also be achieved by GAP models. By contrast, the accuracy of EAM potentials is lower than the DP models and the GAP potentials. Since the free surface formation energies are usually not the fitting target of EAMs, except the MN potential.

The accurate prediction on free surface properties ensures the reliability of the DP models in simulations of surface-related processes, such as cleavage fracture⁷⁸, ad-atom surface diffusion⁷⁹, surface self-assembly⁸⁰ and nano-indentation⁸¹.

C. Grain Boundaries

Grain Boundaries (GBs) are interfaces between differently oriented grains. GBs play dominant roles in many observable properties of W poly-crystals, including textures, radiation resistance and overall mechanical responses to external strain. GB structures are not explicitly presented in the DP training dataset, thus the accuracy of GB formation energy prediction by DP models is mainly guaranteed by the generalizability of the models.

The calculated GB formation energies of the DP-HYB, DP-SE2, EAM potentials, GAP-2 and DFT are presented in Fig.2. The calculated GBs are among the most frequently investigated symmetric tilt GBs: $\Sigma 3$ -(111), $\Sigma 5$ -(012), $\Sigma 5$ -(013) and $\Sigma 3$ -(112). DP-HYB shows good agreement with DFT on all GBs presented in Fig.2. The accuracy of the DP-SE2 is comparable to DP-HYB in most cases, except the $\Sigma 3$ -(111) GB, in which DP-SE2 presents a larger deviation from DFT than all other potentials. The DP-HYB is more accurate than all other EAMs on the formation energies of $\Sigma 3$ -(111) GB and $\Sigma 3$ -(112) GB. For $\Sigma 5$ GBs,

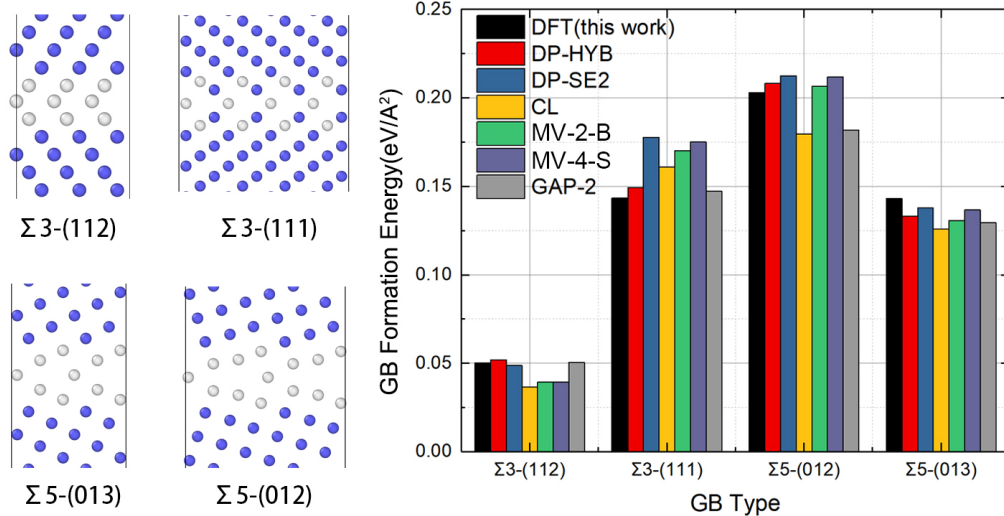


FIG. 2: GB structures and formation energies predicted by DP models in comparison with DFT value (in this work) and other interatomic potential calculated values. Atoms are colored according to the results of common neighbor analysis: atoms in BCC lattice are colored blue and the atoms near the GB is colored gray.

all potentials show good agreement with DFT, thus DP-HYB has no obvious advantages. Although not considering GBs in their database, GAP-2 also have a good prediction on the GB formation energies.

D. Point Defects and Prismatic Loops

The formation energy of SIAs and a vacancy are shown in Table IV. Three dumbbell (db) SIA configurations, i.e. $\langle 111 \rangle$, $\langle 110 \rangle$ and $\langle 100 \rangle$, are investigated. The DP-SE2 presents that the formation energy of $\langle 111 \rangle$ dumbbell is only 0.09 eV lower than that of $\langle 110 \rangle$ dumbbell, which does not agree with DFT calculations showing that the $\langle 111 \rangle$ dumbbell is roughly 0.3 eV more stable than the $\langle 110 \rangle$ dumbbell. The disagreement should be attributed to the limited representability of only using two-body embedding in the descriptor, since the accuracy of DP-SE2 cannot be improved by using larger networks, more training data nor longer training procedure. DP-HYB, by contrast, correctly predicts the formation energy

TABLE IV: Formation energy of differently oriented interstitial dumbbells and mono-vacancy predicted by EAM potentials, GAP models, and DP models. (units: eV)

Type	AT ⁷⁰	JW ²³	MV-2-B ²⁶	MV-4-S ²⁷	MN ²⁸	CL ³¹	GAP-1 ⁴⁴	GAP-2 ⁴⁵	DP-SE2	DP-HYB	DFT _(this work)	Reference
$\langle 111 \rangle$ db	8.92	9.52	10.4	10.4	8.97	9.46	-	10.39	9.68	9.82	9.91	9.55 ⁸² , 10.44 ⁸³
$\langle 110 \rangle$ db	9.62	10.18	10.86	10.89	9.68	9.8	-	10.60	9.77	10.17	10.25	9.84 ⁸² , 10.82 ⁸³
$\langle 100 \rangle$ db	9.8	10.3	10.46	12.81	9.8	11.01	-	12.11	11.45	11.70	11.96	11.49 ⁸² , 12.87 ⁸³
Vacancy	3.63	3.63	3.49	3.82	3.73	3.54	3.29	3.32	3.84	3.30	3.24	3.56 ⁸² , 3.24 ⁴⁸

difference between the dumbbell structures, we believe it is due to the better resolution of the bond-angle contribution in the atomic local environment in SIA structures, making it possible to distinguish different SIA structures. The point-defect formation energies of W are the main fitting targets of EAM potentials and GAP-2. Thus, although maintaining a satisfactory accuracy, DP-HYB has no obvious advantage on this property over the existing potentials.

The interaction between the first-nearest-neighbor (1NN) vacancies is reported to be repulsive (with binding energy, $E_b(1NN) = -0.1$ eV⁸⁴) or weakly attractive ($E_b(1NN) = 0.048$ eV²⁸), but that of the second-nearest-neighbor (2NN) vacancies is shown to be strongly repulsive ($E_b(2NN) = -0.35$ eV⁸⁵, -0.286 eV²⁸). By DP-HYB, E_b between the 1NN vacancies is 0.069 eV, and between 2NN vacancies the E_b is -0.303 eV. The di-vacancy configurations are not explicitly included in the training dataset of DP-HYB. GAP-2 explicitly includes the 1NN and 2NN di-vacancies in their training database and can accurately reproduce the DFT calculation⁴⁵. Evaluating the 1NN and 2NN vacancy interactions have long been a challenge to the empirical potentials. Among them, the MN potential predicts qualitatively correct binding energies as $E_b(1NN) = 0.17$ eV and $E_b(2NN) = -0.13$ eV²⁸.

Although point defect properties are important indicators of potential quality, individual point defects are hardly observable, and the impact of individual point defects to the materials mechanical properties are relatively weak. Instead, their clusters, formed due to the agglomeration of the point defects, may substantially alter the mechanical properties via their interactions with dislocations. Here, we primarily consider two major forms of SIA clusters: prismatic loops and C15-Laves phase clusters.

Prismatic loops are the most common configurations of SIA clusters, and are frequently observed in experiments⁸⁶. Prismatic loops in BCC metals can be categorized into two types according to their Burgers vectors, as shown in Fig.3c, the $1/2\langle 111 \rangle$ loop and the $\langle 100 \rangle$ loop⁸⁷, with the latter playing a more important role in radiation induced hardening at service temperatures due to its lower diffusivity⁸⁸. Fig. 3a shows that the formation energies of $\langle 111 \rangle$ and $\langle 100 \rangle$ prismatic loops predicted by the DP-HYB model are in good agreement with the DFT extrapolation by a discrete-continuum(DC) model⁸⁹. It is noted that large prismatic loops cannot be calculated directly via DFT, thus are not presented in the training data. The accurate prediction of the formation energies demonstrates the DP-HYB’s generalizability to large defect clusters.

Liu et. al. pointed out that most EAM potentials are not able to accurately evaluate the relative stability of large loops³⁰. We plot the loop formation energies predicted by CL, MV-2-B and MV-4-S in Fig. 3b for comparisons. All the EAM models have similar predictions of formation energies of the $\langle 100 \rangle$ loops. The MV-2-B and MV-4-S potentials predict that the $1/2\langle 111 \rangle$ loop is less stable than $\langle 100 \rangle$, which is contradictory to the DFT extrapolation. The AT potential (not shown in Fig. 3) gives nearly equal formation energies of the $1/2\langle 111 \rangle$ and the $\langle 100 \rangle$ loops, JW and MN EAM potentials (not shown in Fig. 3) may predict the correct relative stability of the two loops, but the difference between the formation energies of loops are too small to distinguish the two types of loops³⁰. The CL potential, as the only exception of the EAM potentials, gives qualitatively correct formation energy of the $\langle 111 \rangle$ loop and the correct relative stability, but the accuracy of the $\langle 100 \rangle$ loop formation energy is lower than that of the DP-HYB model. GAP-2 potential benefits from the enhanced generalizability due to the consideration of SIA-clusters, thus may also well predict the relative stability of the $\langle 111 \rangle$ loop and $\langle 100 \rangle$ loop. The formation energies of either prismatic loops or individual self-interstitial atoms is out of the concern in the database the GAP-1, nor did its reference paper present loop formation energies.

In addition, we used the DP models to predict the formation energy of a C15-Laves phase self-interstitial cluster, whose structure is not explicitly presented in the training dataset. The C15-Laves phase cluster is a unique type of SIA cluster other than the prismatic loops, and is able to transform into either type of the prismatic loops⁹⁰. Unlike the case in BCC Fe⁴⁸, the C15 cluster in BCC W is never the stablest configuration at any cluster size. This

is predicted by both the DP model and the DFT extrapolation, see Fig. 3. C15 Laves phase cluster can also be correctly predicted by GAP-2, since the C15 structure is explicitly presented in the database of GAP-2.

The SIA clusters, such as the two-dimensional prismatic loops and the relative ordered three-dimensional C15-Laves phase clusters, are blind to the DP-HYB model, thus the ability of accurately predicting the formation energies of the clusters is mainly attributed to the generalizability of the DP-HYB model and the training dataset. The correct prediction of formation energy proves the DP-HYB model to be reliable candidate potential for simulating the SIA defect cluster evolution, which is critical to the post-irradiation micro-structure.

E. Generalized Stacking Faults

The generalized stacking fault (GSF) energy landscape is defined as the variation of energy on displacing one part of the crystal against the other on a specific plane (γ plane). The GSF energy has strong implications on the possible slip systems of a crystal⁹¹ and the existence of meta-stable stacking faults. GSF energy along a specific direction is referred to as γ -line. We calculate the GSF energies by using the DP models and other EAM/GAP models along the $\langle 111 \rangle$ direction of the $(1\bar{1}2)$ γ plane and $(1\bar{1}0)$ γ plane, and compare the γ -lines with those calculated by DFT in Fig. 4. In order to reproduce the GSF energy of CL potential reported by Chen et. al.³¹, we have to use the un-relaxed GSF energies, while for all the other potential models and the DFT calculation we use the relaxed GSF energies. The relaxed γ -lines of CL potential are also plotted for comparison.

The γ -lines predicted by both DP models are in good agreement with DFT. The EAM predictions of the γ -lines are somehow lower than DFT at the $(1\bar{1}0)$ γ plane and the $(1\bar{1}2)$ γ plane. The γ -lines are also well presented in the training datasets of GAP-1 model, but are omitted by the GAP-2 model. According to ref.⁴⁴, GAP-1 may well-predict the γ -line, but we observe a significant overestimation of γ -line by GAP-2 in Fig. 4.

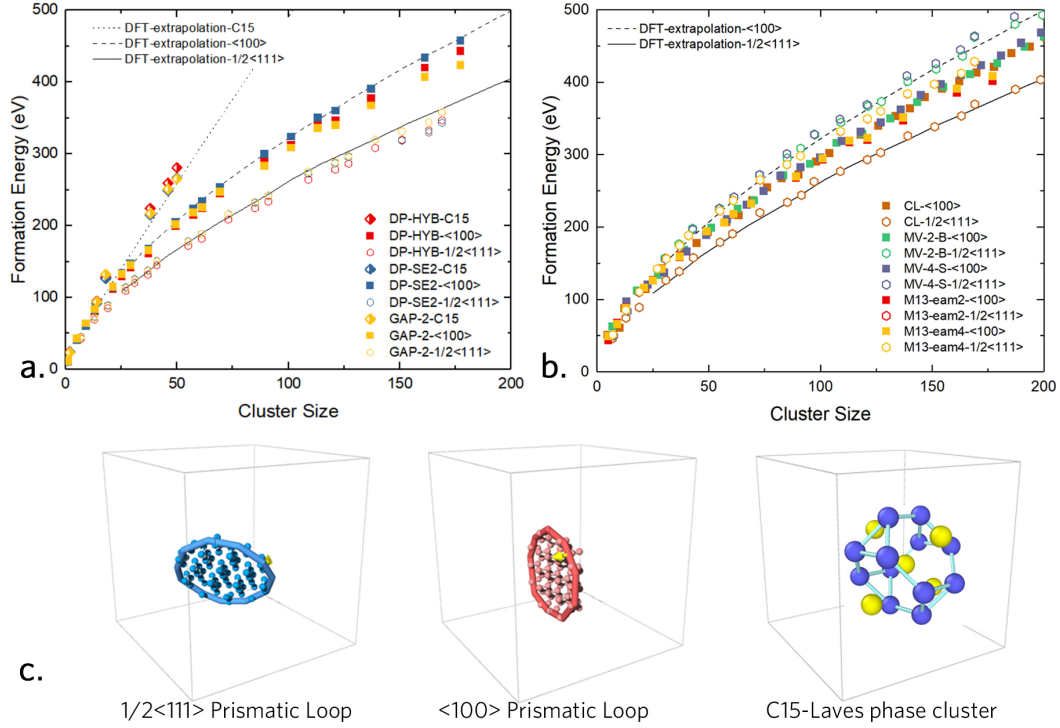


FIG. 3: Prediction of formation energies of $1/2\langle 111 \rangle$, $\langle 100 \rangle$ prismatic loops and C15-Laves phase cluster by DP-HYB model. Comparison is made among the DP models, DFT extrapolation⁸⁹ and EAM potentials. a) Formation energy of $1/2\langle 111 \rangle$, $\langle 100 \rangle$ loops and C15-Laves phase clusters predicted by DP-HYB, DP-SE2 and GAP-2 potential. b) Formation energy of $1/2\langle 111 \rangle$ and $\langle 100 \rangle$ loops predicted by EAM potentials. Note that MV-2-B and MV-4-S potentials are modified from Marinica-13 (M13) EAM-2 and EAM-4, respectively. The predictions of $1/2\langle 111 \rangle$ loops by the M13-EAM-2 and M13-EAM-4 models almost overlap with each other. c) The structures of $1/2\langle 111 \rangle$, $\langle 100 \rangle$ loops and C15-Laves phase clusters in BCC W.

F. Screw Dislocation

In the BCC metals, dislocations are the main carriers of plastic deformation⁹². Plastic deformation in W is dominated by the slow-moving screw dislocation at up to modest temperature⁴². The high migration barrier leads to the low mobility of the screw dislocation, which further determines many key features of the mechanical properties⁹³. For example, in pure W the screw dislocation migration takes a thermally activated "kink-pair" formation

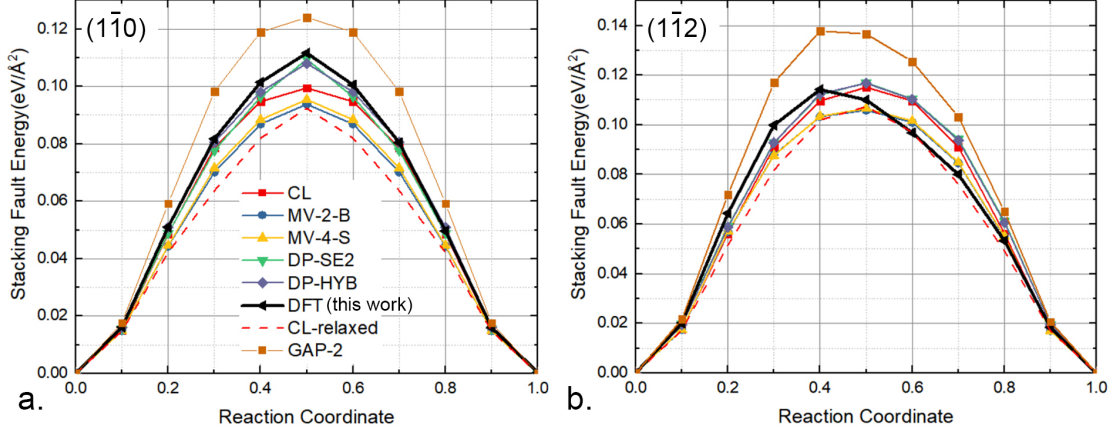


FIG. 4: Prediction of generalized stacking fault energy along $\langle 111 \rangle$ direction on a) $(1\bar{1}0)$ and b) $(1\bar{1}2)$ plane.

mechanism⁹⁴ with an activation energy of 1.7-2.1 eV²¹, leading to low mobility at room temperature. This critical feature is determined by the core structure of screw dislocation, which may also significantly affect the possible slip planes²⁹. Therefore, for the purpose of investigating the mechanical properties of W, an accurate description of the core structure is the fundamental requirement for the interatomic potential.

A schematic illustration of the system we used to calculate the core structure of the screw dislocation using DFT is presented in Fig. 5 (a). The system is composed of 135 atoms with 2 screw dislocations aligned in opposite directions in a dipole arrangement⁴⁴. The dislocation Burgers vectors are $[111]$, and $[\bar{1}\bar{1}\bar{1}]$, respectively. The dipole arrangement ensures the periodic boundary condition applied to all dimensions. The same configuration is used to calculate the Peierls barriers with interatomic potentials. These screw dislocation structures are not included in the training database of the DP models.

In Fig. 5 (b), the differential displacement map (DD-map) and Nye tensor distribution near the screw dislocation cores obtained by the DFT, DP-HYB, DP-SE2, CL/MV-2-B EAM potentials and GAP-2 are presented. The DP-HYB model predicts that the screw dislocation in BCC W exhibits a non-planar, non-degenerate core structure with three-fold symmetry, and the dislocation core does not spread towards three nearby $\langle 112 \rangle$ directions. The dislocation core structure of the DP-HYB model is in satisfactory agreement with our

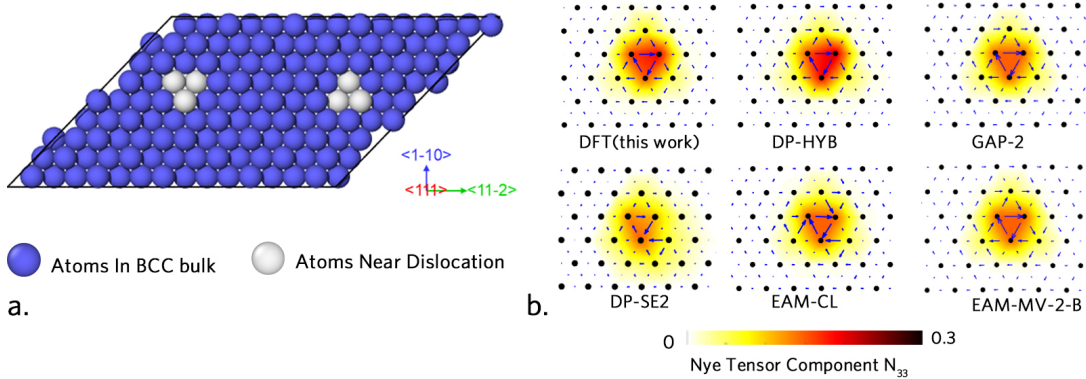


FIG. 5: a) Schematics illustration for the dipole arrangement used for calculating the core-structure of screw dislocation in DFT simulations. b) Differential displacement vector and nye-tensor distribution for ground-state screw dislocation core structure predicted by DFT, DP-HYB, DP-SE2, CL, MV-2-B and GAP-2 potentials.

DFT calculation and other DFT results reported in literature^{46,95,96}. The MV-2-B and MV-4-S potentials are able to predict correct core structure as well^{26,27}. The GAP-1 potential explicitly includes the dislocation structures in its training dataset, thus being able to predict the correct core structure. The GAP-2 potential does not explicitly consider the screw dislocation structures in their training dataset, and is able to predict the correct screw core structure. By contrast, DP-SE2 predicts a split-core structure, and the CL EAM potential gives a hard-core structure, which are inconsistent with the DFT calculations.

The intrinsic migration barrier per unit length of screw dislocation, named the Peierls barrier, determines the mobility of screw dislocation. We calculate the minimum-energy-path (MEP) of screw dislocation migration by the nudged-elastic-band (NEB)⁹⁷ method, and present the MEPs in Fig. 6 (a). The DP-HYB model gives a Peierls barrier of 84 meV/b, which is in good agreement with the DFT calculations ranging from 70meV/b to 105meV/b^{21,44,46} and our DFT calculation result 89 meV/b. By contrast, the prediction of DP-SE2 on Peierls barrier is drastically lower than the reference DFT values. We attribute the unphysical prediction of DP-SE2 to the lack of representability, because the DP-SE2 could not be improved by explicitly including the configurations along the MEP path in the training dataset. This drawback is significantly improved by the three-body embedding for-

malism employed in the DP-HYB model. The MV-2-B and MV-4-S EAM potentials predict Peierls barriers of 54 and 62 meV/b, respectively. The GAP-1 potential also has a good prediction on the Peierls barrier⁴⁴, since it considered the screw dislocation structure in the dataset. The GAP-2 potential, however, omitted the screw dislocation properties for the purpose of keeping the dataset relatively small to reuse in other BCC metals⁴⁵ (see ref.⁹⁸ for GAP potentials for V, Mo and Ta et. al.), thus predicted a lower Peierls barrier than GAP-1 and the DFT references.

The dislocation core structures of the DFT, DP-HYB and DP-SE2 at the initial, saddle and final states of the migration path are plotted and compared in Fig. 6 (c). DP-HYB is able to predict the correct ground-state three-fold core structure, and the split-core structure at the saddle point. DP-SE2 disagrees with DFT on core-structure at the saddle point.

A special feature of BCC metals is the break down of Schmid-Law, namely the yield stress of BCC metals under mechanical loading depends not only on the orientation of the shear plane, resulting in the so-called twining/anti-twinning (T/AT) asymmetry⁹⁹. This asymmetry is physically connected to the departure of the dislocation migration MEP away from the straight path connecting two nearby non-degenerate core positions¹⁰⁰. To test whether the non-schmid effect can be predict by the DP-HYB model, we extracted the dislocation core trajectory along the MEP via the cost-function method^{46,101}. The trajectory of the dislocation core calculated by DP-HYB is close the DFT calculation⁹⁹, as is observed from Fig. 6 (b). This indicates that the non-Schmid effect can be correctly exhibited in the simulations using the DP-HYB model. Since the DP-SE2 does not present the reasonable core structure and Peierls barrier, the dislocation trajectory calculation for DP-SE2 is not presented. Again, it should be emphasized no screw dislocation structure is presented in the training database of the DP-HYB model, thus the accurate prediction of these properties is mainly attributed to the generalizability of the model. The agreement with DFT on screw dislocation core structure, Peierls barrier, and dislocation trajectory, proves that the DP-HYB model is reliable for simulating the screw dislocation-dominated plastic deformation under mechanical load.

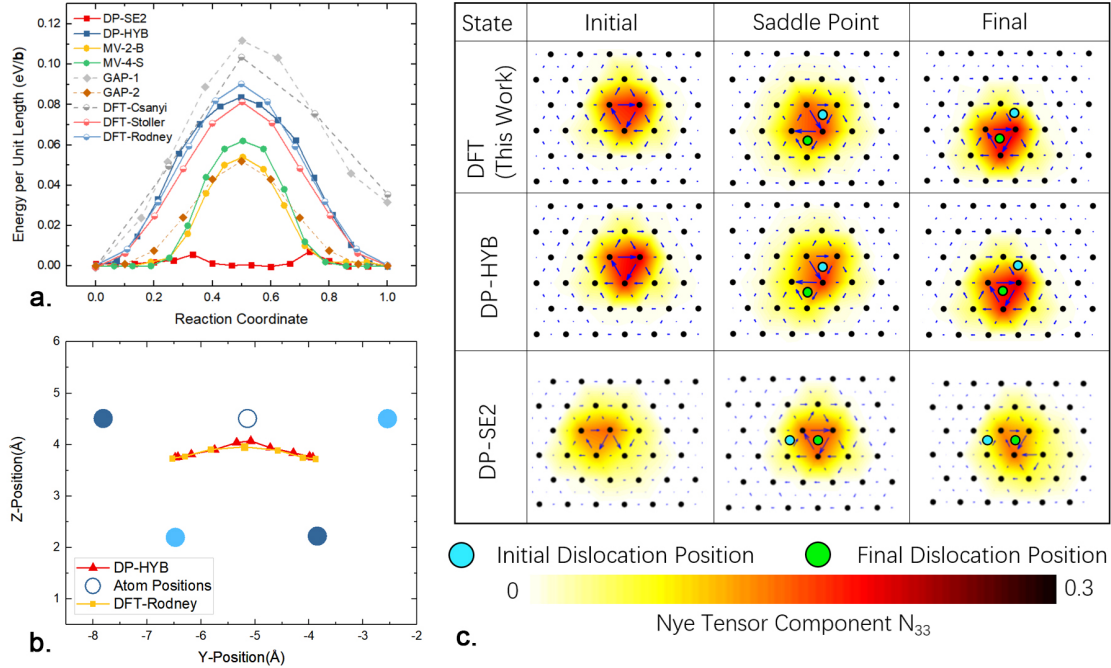


FIG. 6: a) Peierls barrier obtained by DFT, DP-HYB and DP-SE2 models, EAM models, GAP models and reference DFT values, respectively. We also take DFT calculated Peierls barriers by Rodney et al⁴⁶, Csanyi⁴⁴ et al. and Stoller⁹⁶ et al as references. DP-HYB can predict the correct Peierls barrier value 84 meV/b, which is close to DFT calculated results, but the DP-SE2 model fails to reproduce Peierls barrier value. b) Screw dislocation trajectory along its MEP predicted by DP-HYB model and previous DFT⁴⁶. c) Dislocation core structure DD-maps along their transition path predicted by DFT and DP models. DP-HYB can predict the correct ground-state dislocation core structure, and well reproduces the core structure at saddle point.

G. Efficiency

In order to benchmark the efficiency of the ML potentials, we conduct MD simulations in a 128 atom, $3 \times 3 \times 3$ BCC W supercell, using DP-HYB, DP-SE2 and GAP-2, CL and a MEAM potential proposed by Lee et al.¹⁰². The DP-SE2 model is highly optimized for the GPU architecture¹⁰³, but such optimization is only partially available for DP-HYB and not available for the GAP-2 model. Therefore, for an unbiased comparison, we only use one core of an Intel Xeon Platinum 8269CY CPU to benchmark all models, and the results are

TABLE V: The computational efficiency of the CL, MEAM, DP-SE2, DP-HYB and GAP-2 models. The total wall clock time are recorded for 1×10^5 times steps MD simulations of a system consisting 128 atoms. Only one core of an Intel(R) Xeon(R) Platinum 8269CY CPU @ 2.50GHz is used in all test cases.

Potential	CL	MEAM ¹⁰²	DP-SE2	DP-HYB	GAP-2
Time(ms/step/atom)	0.002	0.009	0.657	1.475	4.584

shown in Table V. The hybridization of the descriptors makes the DP-HYB 1.6 times more expensive than DP-SE2 model. The DP-HYB model is more than 3 times faster than GAP-2 potential. Since the size of the database of GAP-2 is smaller than GAP-1, we would expect that the GAP-1 model is more expensive than the GAP-2 model. It is noted that with the recently developed model compression technique, the performance of the DP-SE2 model is further improved up to a factor of 10 with respect to the highly optimized GPU code¹⁰⁴, which makes the efficiency of the DP-SE2 model comparable to the MEAM potentials. The efficiency of the DP-HYB model will benefit from the same model compression techniques in the near future, and be made more suitable for large-scale atomistic simulations.

IV. CONCLUSIVE REMARKS

In this work, a highly generalizable (in the sense of in-distribution) W deep neural-network potential is developed for the purpose of reliable atomistic simulations of property degradation of tungsten that serves under complex multi-physics working condition in the fusion facilities. This potential utilizes a newly designed descriptor: DP-HYB, which consists of a three-body-embedding descriptor and the original two-body-embedding descriptor. The representability of the DP-HYB model is significantly enhanced due to the explicit consideration of bond-angle contribution in the embedding matrix. With the excellent fitting ability of the deep neural networks, the DP-HYB model is fitted to over 40000 configurations generated by the concurrent learning scheme DP-GEN.

According to our benchmark results, the three-body embedding formalism enables the

W DP-HYB potential to achieve the accurate description of a wide range of properties including bulk, elastic, defective properties such as formation energies of free surfaces and grain boundaries, GSF energies, formation energies of prismatic loops, screw dislocation core structure, Peierls barrier and migration trajectory. Only the elastically deformed lattice structures, DP-GEN explored bulk and free surfaces, SIA dumbbell, mono-vacancy and GSF structures are explicitly included in the training dataset, so the correct prediction of the other properties is attributed to the generalizability of the DP-HYB model. It is noted that the correct prediction of all the benchmarked properties with the same model is by far challenging for the empirical and ML potential models, including the original DP model that only uses the two-body embedding. Therefore, the DP-HYB is believed a good candidate potential for revealing the underlying physics of mechanical property degradation of W serving under the multi-physics environment.

Although the representability and generalizability of the DP-HYB model are satisfactory, it is unlikely that the current version can be used to simulate the procedures like the early stage of primary irradiation damage formation, because in the present work the DFT calculation settings are not suitable for very short-range atomistic interactions, so will fail in predicting the dynamics of atomic collisions with high speed. To improve the performance in this specific field, coupling with the short-range repulsion models, in a way like the DP-ZBL¹⁰⁵ model does, is suggested. GAP-2 is suitable for simulating early-stage primary radiation damage formation processes, because it is specially fitted to the short-range repulsive interaction between W. The extension of the DP-HYB model to the simulation of primary irradiation damage is beyond the scope of the current work, and will be investigated in future works.

In addition, due to previous successes of the DP model in binary and ternary alloys, our future goals include investigating the defect behavior under the influence of alloying/impurity elements. For example, the effect of Rhenium on the stacking fault energy and screw dislocation core structures, the effect of interstitial impurities on the formation energies of screw dislocation kink-pairs and the grain boundary segregation, the formation of hydrogen blisters and precipitates. Atomistic simulations of these critical behaviors can be informative to the design of alloys that serves in the multi-physics environment. Besides W, we believe that DP-HYB formalism can also have wide prospects of application of other engineering

materials and alloys that serve under complex and harsh conditions.

V. DATA AVAILABILITY

The DP models, the training dataset and the scripts used to produce the results are available at <https://doi.org/10.5281/zenodo.6466996>. The DP models and the training data are also available at https://dplibrary.deepmd.net/#/project_details?project_id=202204.002.

Acknowledgement

The work is supported by the National Science Foundation of China under Grant No.11871110 and 12122103.

* Electronic address: wang_han@iapcm.ac.cn

¹ Steven J Zinkle, Anton Möslang, Takeo Muroga, and H Tanigawa. Multimodal options for materials research to advance the basis for fusion energy in the iter era. *Nuclear Fusion*, 53(10):104024, 2013.

² Rion Causey, Ken Wilson, Tom Venhaus, and W R Wampler. Tritium retention in tungsten exposed to intense fluxes of 100 ev tritons. *Journal of Nuclear Materials*, 266:467–471, 1999.

³ H Bolt, V Barabash, W Krauss, J Linke, R Neu, S Suzuki, N Yoshida, and ASDEX Upgrade Team. Materials for the plasma-facing components of fusion reactors. *Journal of nuclear materials*, 329:66–73, 2004.

⁴ R Neu, V Bobkov, R Dux, A Kallenbach, Th Pütterich, H Greuner, O Gruber, A Herrmann, Ch Hopf, K Krieger, et al. Final steps to an all tungsten divertor tokamak. *Journal of nuclear materials*, 363:52–59, 2007.

⁵ K Wittlich, T Hirai, J Compan, N Klimov, J Linke, A Loarte, M Merola, G Pintsuk, V Podkovyrov, L Singheiser, et al. Damage structure in divertor armor materials exposed to multiple iter relevant elm loads. *Fusion engineering and design*, 84(7-11):1982–1986, 2009.

- ⁶ M Rieth, Sergei L Dudarev, SM Gonzalez De Vicente, J Aktaa, T Ahlgren, S Antusch, DEJ Armstrong, M Balden, Nadine Baluc, M-F Barthe, et al. Recent progress in research on tungsten materials for nuclear fusion applications in europe. *Journal of Nuclear Materials*, 432(1-3):482–500, 2013.
- ⁷ Xunxiang Hu, Takaaki Koyanagi, Makoto Fukuda, NAP Kiran Kumar, Lance L Snead, Brian D Wirth, and Yutai Katoh. Irradiation hardening of pure tungsten exposed to neutron irradiation. *Journal of Nuclear Materials*, 480:235–243, 2016.
- ⁸ Akira Hasegawa, Takashi Tanno, Shuhei Nogami, and Manabu Satou. Property change mechanism in tungsten under neutron irradiation in various reactors. *Journal of nuclear materials*, 417(1-3):491–494, 2011.
- ⁹ Steven J Zinkle and Jeremy T Busby. Structural materials for fission & fusion energy. *Materials today*, 12(11):12–19, 2009.
- ¹⁰ Yuri N Osetsky. Atomic-scale mechanisms of void strengthening in tungsten. *Tungsten*, 3(1):65–71, 2021.
- ¹¹ A.S. Arakcheev, A. Huber, M. Wirtz, G. Sergienko, I. Steudel, A.V. Burdakov, J.W. Coenen, A. Kreter, J. Linke, Ph. Mertens, A.A. Shoshin, B. Unterberg, and A.A. Vasilyev. Theoretical investigation of crack formation in tungsten after heat loads. *Journal of Nuclear Materials*, 463:246–249, 2015. PLASMA-SURFACE INTERACTIONS 21.
- ¹² Hanns Gietl, Takaaki Koyanagi, Xunxiang Hu, Makoto Fukuda, Akira Hasegawa, and Yutai Katoh. Neutron irradiation-enhanced grain growth in tungsten and tungsten alloys. *Journal of Alloys and Compounds*, 901:163419, 2022.
- ¹³ Linfeng Zhang, De-Ye Lin, Han Wang, Roberto Car, and Weinan E. Active learning of uniformly accurate interatomic potentials for materials simulation. *Physical Review Materials*, 3(2):023804, 2019.
- ¹⁴ MW Finnis and JE Sinclair. A simple empirical n-body potential for transition metals. *Philosophical Magazine A*, 50(1):45–55, 1984.
- ¹⁵ GJ Ackland and R Thetford. An improved n-body semi-empirical model for body-centred cubic transition metals. *Philosophical Magazine A*, 56(1):15–30, 1987.
- ¹⁶ RA Johnson and DJ Oh. Analytic embedded atom method model for bcc metals. *Journal of Materials Research*, 4(5):1195–1201, 1989.
- ¹⁷ SM Foiles. Interatomic interactions for mo and w based on the low-order moments of the

- density of states. *Physical Review B*, 48(7):4287, 1993.
- ¹⁸ XD Dai, JH Li, and Y Kong. Long-range empirical potential for the bcc structured transition metals. *Physical Review B*, 75(5):052102, 2007.
- ¹⁹ Peter M Derlet, D Nguyen-Manh, and SL Dudarev. Multiscale modeling of crowdion and vacancy defects in body-centered-cubic transition metals. *Physical Review B*, 76(5):054107, 2007.
- ²⁰ Jun Wang, YL Zhou, Min Li, and Qing Hou. A modified w-w interatomic potential based on ab initio calculations. *Modelling and Simulation in Materials Science and Engineering*, 22(1):015004, 2013.
- ²¹ Mihai-Cosmin Marinica, Lisa Ventelon, MR Gilbert, L Proville, SL Dudarev, J Marian, G Benteux, and F Willaime. Interatomic potentials for modelling radiation defects and dislocations in tungsten. *Journal of Physics: Condensed Matter*, 25(39):395502, 2013.
- ²² Kleber Carlos Mundim, LAC Malbouisson, Simon Dorfman, D Fuks, Jan Van Humbeeck, and Vlad Liubich. Diffusion properties of tungsten from atomistic simulations with ab initio potentials. *Journal of Molecular Structure: THEOCHEM*, 539(1-3):191–197, 2001.
- ²³ N Juslin and BD Wirth. Interatomic potentials for simulation of he bubble formation in w. *Journal of Nuclear Materials*, 432(1-3):61–66, 2013.
- ²⁴ Mitchell A. Wood and Aidan P. Thompson. Quantum-accurate molecular dynamics potential for tungsten, 2017.
- ²⁵ Michael I Baskes. Modified embedded-atom potentials for cubic materials and impurities. *Physical review B*, 46(5):2727, 1992.
- ²⁶ G. Bonny, A. Bakaev, D. Terentyev, and Yu. A. Mastrikov. Interatomic potential to study plastic deformation in tungsten-rhenium alloys. *Journal of Applied Physics*, 121(16):165107, 2017.
- ²⁷ W. Setyawan, N. Gao, and Richard J Kurtz. A tungsten-rhenium interatomic potential for point defect studies. *Journal of Applied Physics*, 123(20):205102, 2018.
- ²⁸ D R Mason, D Nguyen-Manh, and C S Becquart. An empirical potential for simulating vacancy clusters in tungsten. *Journal of Physics: Condensed Matter*, 29(50):505501, nov 2017.
- ²⁹ G Bonny, D Terentyev, A Bakaev, P Grigorev, and D Van Neck. Many-body central force potentials for tungsten. *Modelling and Simulation in Materials Science and Engineering*, 22(5):053001, jun 2014.

- ³⁰ L. X. Liu, X. C. Li, Y. C. Chen, W. Y. Hu, and H. Q. Deng. Evaluation of tungsten interatomic potentials for radiation damage simulations. *Tungsten*, 2(1):3–14, 2020.
- ³¹ Y. Chen, Y. H. Li, N. Gao, H. B. Zhou, W. Hu, G. H. Lu, F. Gao, and H. Deng. New interatomic potentials of w, re and w-re alloy for radiation defects. *Journal of Nuclear Materials*, pages 141–153, 2018.
- ³² Aidan P Thompson, Laura P Swiler, Christian R Trott, Stephen M Foiles, and Garritt J Tucker. Spectral neighbor analysis method for automated generation of quantum-accurate interatomic potentials. *Journal of Computational Physics*, 285:316–330, 2015.
- ³³ Alexander V Shapeev. Moment tensor potentials: A class of systematically improvable interatomic potentials. *Multiscale Modeling & Simulation*, 14(3):1153–1173, 2016.
- ³⁴ Jörg Behler and Michele Parrinello. Generalized neural-network representation of high-dimensional potential-energy surfaces. *Physical Review Letters*, 98(14):146401, 2007.
- ³⁵ Albert P Bartók, Mike C Payne, Risi Kondor, and Gábor Csányi. Gaussian approximation potentials: The accuracy of quantum mechanics, without the electrons. *Physical Review Letters*, 104(13):136403, 2010.
- ³⁶ Stefan Chmiela, Alexandre Tkatchenko, Huziel E Sauceda, Igor Poltavsky, Kristof T Schütt, and Klaus-Robert Müller. Machine learning of accurate energy-conserving molecular force fields. *Science Advances*, 3(5):e1603015, 2017.
- ³⁷ Kristof Schütt, Pieter-Jan Kindermans, Huziel Enoc Sauceda Felix, Stefan Chmiela, Alexandre Tkatchenko, and Klaus-Robert Müller. Schnet: A continuous-filter convolutional neural network for modeling quantum interactions. In *Advances in Neural Information Processing Systems*, pages 992–1002, 2017.
- ³⁸ Justin S Smith, Olexandr Isayev, and Adrian E Roitberg. ANI-1: an extensible neural network potential with DFT accuracy at force field computational cost. *Chemical Science*, 8(4):3192–3203, 2017.
- ³⁹ Jiequn Han, Linfeng Zhang, Roberto Car, and Weinan E. Deep potential: a general representation of a many-body potential energy surface. *Communications in Computational Physics*, 23(3):629–639, 2018.
- ⁴⁰ Linfeng Zhang, Jiequn Han, Han Wang, Roberto Car, and Weinan E. Deep potential molecular dynamics: A scalable model with the accuracy of quantum mechanics. *Physical Review Letters*, 120:143001, 2018.

- ⁴¹ Linfeng Zhang, Jiequn Han, Han Wang, Wissam A Saidi, Roberto Car, and Weinan E. End-to-end symmetry preserving inter-atomic potential energy model for finite and extended systems. In *Advances of the Neural Information Processing Systems (NIPS)*, 2018.
- ⁴² F. Maresca, D. Dragoni, G Csanyi, N. Marzari, and W. A. Curtin. Screw dislocation structure and mobility in body centered cubic fe predicted by a gaussian approximation potential. *Npj Computational Materials*, 4(1), 2018.
- ⁴³ AP Bartok, M. C. Payne, R. Kondor, and G Csányi. Gaussian approximation potentials: The accuracy of quantum mechanics, without the electrons. *Physical Review Letters*, 104(13):136403, 2012.
- ⁴⁴ W. J. Szlachta, AP Bartók, and G Csányi. Accuracy and transferability of gaussian approximation potential models for tungsten. *Phys.rev.b*, 90(10):104108, 2014.
- ⁴⁵ Jesper Byggmästar, Ali Hamedani, Kai Nordlund, and Flyura Djurabekova. Machine-learning interatomic potential for radiation damage and defects in tungsten. *Physical Review B*, 100(14):144105, 2019.
- ⁴⁶ Lisa Ventelon, F. Willaime, E. Clouet, and D. Rodney. Ab initio investigation of the peierls potential of screw dislocations in bcc fe and w. *Acta Materialia*, 61(11):3973–3985, 2013.
- ⁴⁷ Xiaowang Wang, Shuozhi Xu, Wu-Rong Jian, Xiang-Guo Li, Yanqing Su, and Irene J Beyerslein. Generalized stacking fault energies and peierls stresses in refractory body-centered cubic metals from machine learning-based interatomic potentials. *Computational Materials Science*, 192:110364, 2021.
- ⁴⁸ Alexandra M. Goryaeva, Julien Dérès, Clovis Lapointe, Petr Grigorev, Thomas D. Swinburne, James R. Kermode, Lisa Ventelon, Jacopo Baima, and Mihai-Cosmin Marinica. Efficient and transferable machine learning potentials for the simulation of crystal defects in bcc fe and w. *Phys. Rev. Materials*, 5:103803, Oct 2021.
- ⁴⁹ W. Jiang, Y. Zhang, L. Zhang, and Han Wang. Accurate Deep Potential model for the Al-Cu-Mg alloy in the full concentration space. *arXiv: Materials Science*, 2020.
- ⁵⁰ L. Zhang, H. Wang, R. Car, and W. E. The phase diagram of a deep potential water model. *arXiv:2102.04804*, 2021.
- ⁵¹ Yinan Wang, Xiaoyang Wang, Linfeng Zhang, Ben Xu, and Han Wang. A generalizable machine-learning potential of ag-au nanoalloys and its application on surface reconstruction, segregation and diffusion. *arXiv preprint arXiv:2108.06232*, 2021.

- ⁵² Daniel Marchand, Abhinav Jain, Albert Glensk, and WA Curtin. Machine learning for metallurgy i. a neural-network potential for al-cu. *Physical Review Materials*, 4(10):103601, 2020.
- ⁵³ Alireza Bahramian. Study on growth rate of tio2 nanostructured thin films: simulation by molecular dynamics approach and modeling by artificial neural network. *Surface and interface analysis*, 45(11-12):1727–1736, 2013.
- ⁵⁴ Tomasz Urbańczyk and Jarosław Koperski. Neural networks and determination of diatomic molecule interatomic potential of cadmium dimer. *Spectrochimica Acta Part A: Molecular and Biomolecular Spectroscopy*, 189:502–509, 2018.
- ⁵⁵ Lin Hu, Rui Su, Bing Huang, and Feng Liu. An accurate and transferable machine-learning interatomic potential for silicon. *arXiv preprint arXiv:1901.01638*, 2019.
- ⁵⁶ Wenwen Li, Yasunobu Ando, and Satoshi Watanabe. Cu diffusion in amorphous ta2o5 studied with a simplified neural network potential. *Journal of the Physical Society of Japan*, 86(10):104004, 2017.
- ⁵⁷ Ryo Kobayashi, Daniele Giofré, Till Junge, Michele Ceriotti, and William A Curtin. Neural network potential for al-mg-si alloys. *Physical Review Materials*, 1(5):053604, 2017.
- ⁵⁸ Nongnuch Artrith and Alexander Urban. An implementation of artificial neural-network potentials for atomistic materials simulations: Performance for tio2. *Computational Materials Science*, 114:135–150, 2016.
- ⁵⁹ Nongnuch Artrith and Jörg Behler. High-dimensional neural network potentials for metal surfaces: A prototype study for copper. *Physical Review B*, 85(4):045439, 2012.
- ⁶⁰ Albert P Bartók, James Kermode, Noam Bernstein, and Gábor Csányi. Machine learning a general-purpose interatomic potential for silicon. *Physical Review X*, 8(4):041048, 2018.
- ⁶¹ John A Moriarty. Analytic representation of multi-ion interatomic potentials in transition metals. *Physical Review B*, 42(3):1609, 1990.
- ⁶² Yuzhi Zhang, Haidi Wang, Weijie Chen, Jinzhe Zeng, Linfeng Zhang, Han Wang, and Weinan E. DP-GEN: A concurrent learning platform for the generation of reliable deep learning based potential energy models. *Computer Physics Communications*, page 107206, 2020.
- ⁶³ Steve Plimpton. Fast parallel algorithms for short-range molecular dynamics. *Journal of Computational Physics*, 117(1):1–19, 1995.
- ⁶⁴ Han Wang, Linfeng Zhang, Jiequn Han, and Weinan E. DeePMD-kit: A deep learning package for many-body potential energy representation and molecular dynamics. *Computer Physics*

- Communications*, 228:178–184, 2018.
- ⁶⁵ John P. Perdew, Kieron Burke, and Matthias Ernzerhof. Generalized gradient approximation made simple. *Physical Review Letters*, 77:3865–3868, 1996.
- ⁶⁶ Georg Kresse and Jürgen Furthmüller. Efficient iterative schemes for ab initio total-energy calculations using a plane-wave basis set. *Physical Review B*, 54(16):11169, 1996.
- ⁶⁷ Georg Kresse and Jürgen Furthmüller. Efficiency of ab-initio total energy calculations for metals and semiconductors using a plane-wave basis set. *Computational Materials Science*, 6(1):15–50, 1996.
- ⁶⁸ Diederik Kingma and Jimmy Ba. Adam: a method for stochastic optimization. In *Proceedings of the International Conference on Learning Representations (ICLR)*, 2015.
- ⁶⁹ Martin Abadi, Ashish Agarwal, Paul Barham, Eugene Brevdo, Zhifeng Chen, Craig Citro, Gregory S Corrado, Andrew Davis, Jeffrey Dean, Matthieu Devin, et al. Tensorflow: Large-scale machine learning on heterogeneous distributed systems. *arXiv: Distributed, Parallel, and Cluster Computing*, 2015.
- ⁷⁰ G. J. Ackland and R. Thetford. An improved n-body semi-empirical model for body-centred cubic transition metals. *Philosophical Magazine A*, 56(1):15–30, 1987.
- ⁷¹ T. Ochs, O. Beck, C. Elsässer, and B. Meyer. Symmetrical tilt grain boundaries in body-centred cubic transition metals: An ab initio local-density-functional study. *Philosophical Magazine A*, 80(2):351–372, 2000.
- ⁷² K. Heinola and T. Ahlgren. Diffusion of hydrogen in bcc tungsten studied with first principle calculations. *Journal of Applied Physics*, 107(11):S203, 2010.
- ⁷³ Gene Simmons. Single crystal elastic constants and calculated aggregate properties. Technical report, Southern Methodist Univ Dallas Tex, 1965.
- ⁷⁴ K. Einarsdotter, B. Sadigh, G. Grimvall, and V. Ozoliņš. Phonon instabilities in fcc and bcc tungsten. *Phys. Rev. Lett.*, 79:2073–2076, Sep 1997.
- ⁷⁵ Hans Landolt and Börnstein. *Landolt-Börnstein: Numerical Data and Functional Relationships in Science and Technology: Refractory Metal Systems*. Springer., 1991.
- ⁷⁶ Lisa Ventelon and F Willaime. Generalized stacking-faults and screw-dislocation core-structure in bcc iron: A comparison between ab initio calculations and empirical potentials. *Philosophical Magazine*, 90(7-8):1063–1074, 2010.
- ⁷⁷ C Kittel. *Introduction to Solid State Physics*. Wiley, New York., 2005.

- ⁷⁸ E. Gaganidze, D. Rupp, and J. Aktaa. Fracture behaviour of polycrystalline tungsten. *Journal of Nuclear Materials*, 446(1-3):240–245, 2014.
- ⁷⁹ Ville Jansson, Andreas Kyritsakis, Simon Vigonski, Ekaterina Baibuz, Vahur Zadin, Alvo Aabloo, and Flyura Djurabekova. Tungsten migration energy barriers for surface diffusion: a parameterization for KMC simulations. *Modelling and Simulation in Materials Science and Engineering*, 28(3):035011, feb 2020.
- ⁸⁰ Jiaxing Wang, Yuzhang Liang, Pengcheng Huo, Daopeng Wang, Jun Tan, and Ting Xu. Large-scale broadband absorber based on metallic tungsten nanocone structure. *Applied Physics Letters*, 111(25):251102, 2017.
- ⁸¹ JHA Hagelaar, E Bitzek, CFJ Flipse, and P Gumbsch. Atomistic simulations of the formation and destruction of nanoindentation contacts in tungsten. *Phys.rev.b*, 73(4):39–59, 2006.
- ⁸² D. Nguyen-Manh, A. Horsfield, and S. Dudarev. Self-interstitial atom defects in bcc transition metals: Group-specific trends. *Physical Review B Condensed Matter*, 73(2):020101, 2006.
- ⁸³ L. Ventelon, F. Willaime, C. C. Fu, M. Heran, and I. Ginoux. Ab initio investigation of radiation defects in tungsten: Structure of self-interstitials and specificity of di-vacancies compared to other bcc transition metals. *Journal of Nuclear Materials*, 425(1-3):16–21, 2012.
- ⁸⁴ C.S. Becquart and C. Domain. Ab initio calculations about intrinsic point defects and he in w. *Nuclear Instruments and Methods in Physics Research Section B: Beam Interactions with Materials and Atoms*, 255(1):23–26, 2007. Computer Simulation of Radiation Effects in Solids.
- ⁸⁵ K. Heinola, F. Djurabekova, and T. Ahlgren. On the stability and mobility of di-vacancies in tungsten. *Nuclear Fusion*, 58(2):026004, dec 2017.
- ⁸⁶ O. El-Atwani, E. Esquivel, M. Efe, E. Aydogan, Y.Q. Wang, E. Martinez, and S.A. Maloy. Loop and void damage during heavy ion irradiation on nanocrystalline and coarse grained tungsten: Microstructure, effect of dpa rate, temperature, and grain size. *Acta Materialia*, 149:206–219, 2018.
- ⁸⁷ H. Xu, R. E. Stoller, Y. N. Osetsky, and D. Terentyev. Solving the puzzle of interstitial loop formation in bcc iron. *Physical Review Letters*, 110(26):265503–265503, 2013.
- ⁸⁸ Abdallah Reza, Hongbing Yu, Kenichiro Mizohata, and Felix Hofmann. Thermal diffusivity degradation and point defect density in self-ion implanted tungsten. *Acta Materialia*, 193:270–279, 2020.
- ⁸⁹ R. Alexander, M. C. Marinica, L. Proville, F. Willaime, K. Arakawa, M. R. Gilbert, and S. L.

- Dudarev. Ab initio scaling laws for the formation energy of nanosized interstitial defect clusters in iron, tungsten, and vanadium. *Physical review. B, Condensed Matter And Materials Physics*, 94(2):024103.1–024103.15, 2016.
- ⁹⁰ Yongfeng Zhang, Xian-Ming Bai, Michael R Tonks, and S Bulent Biner. Formation of prismatic loops from c15 laves phase interstitial clusters in body-centered cubic iron. *Scripta materialia*, 98:5–8, 2015.
- ⁹¹ L. Romaner, C. Ambrosch-Draxl, and R. Pippan. Effect of rhenium on the dislocation core structure in tungsten. *Physical Review Letters*, 104(19):195503, 2010.
- ⁹² Giacomo Po, Yinan Cui, David Rivera, David Cereceda, Tom D. Swinburne, Jaime Marian, and Nasr Ghoniem. A phenomenological dislocation mobility law for bcc metals. *Acta Materialia*, 119:123–135, 2016.
- ⁹³ G D Samolyuk, Y N Osetsky, and R E Stoller. The influence of transition metal solutes on the dislocation core structure and values of the peierls stress and barrier in tungsten. *Journal of Physics: Condensed Matter*, 25(2):025403, nov 2012.
- ⁹⁴ L. Proville, D. Rodney, and M. C. Marinica. Quantum effect on thermally activated glide of dislocations. *Nature Materials*, 11:845–849, 2012.
- ⁹⁵ D Cereceda, A Stukowski, M R Gilbert, S Queyreau, Lisa Ventelon, M-C Marinica, J M Perlado, and J Marian. Assessment of interatomic potentials for atomistic analysis of static and dynamic properties of screw dislocations in w. *Journal of Physics: Condensed Matter*, 25(8):085702, jan 2013.
- ⁹⁶ G. D. Samolyuk, Y. N. Osetsky, and R. E. Stoller. The influence of transition metal solutes on dislocation core structure and values of peierls stress and barrier in tungsten. *J Phys Condens Matter*, 25(2):025403, 2012.
- ⁹⁷ Graeme Henkelman, Blas P. Uberuaga, and Hannes Jónsson. A climbing image nudged elastic band method for finding saddle points and minimum energy paths. *The Journal of Chemical Physics*, 113(22):9901–9904, 2000.
- ⁹⁸ Jesper Byggmästar, Kai Nordlund, and Flyura Djurabekova. Gaussian approximation potentials for body-centered-cubic transition metals. *Physical Review Materials*, 4(9):093802, 2020.
- ⁹⁹ Antoine Kraych, Emmanuel Clouet, Lucile Dezerald, Lisa Ventelon, François Willaime, and David Rodney. Non-glide effects and dislocation core fields in bcc metals. *npj Computational Materials*, 5(1):1–8, 2019.

- ¹⁰⁰ L. Dezerald, D. Rodney, E. Clouet, L. Ventelon, and Francois Willaime. Plastic anisotropy and dislocation trajectory in bcc metals. *Nature Communications*, 7(1):11695, 2016.
- ¹⁰¹ L Dezerald, Lisa Ventelon, E Clouet, C Denoual, David Rodney, and F Willaime. Ab initio modeling of the two-dimensional energy landscape of screw dislocations in bcc transition metals. *Physical Review B*, 89(2):024104, 2014.
- ¹⁰² Byeong-Joo Lee, MI Baskes, Hanchul Kim, and Yang Koo Cho. Second nearest-neighbor modified embedded atom method potentials for bcc transition metals. *Physical Review B*, 64(18):184102, 2001.
- ¹⁰³ Weile Jia, Han Wang, Mohan Chen, Denghui Lu, Lin Lin, Roberto Car, E Weinan, and Linfeng Zhang. Pushing the limit of molecular dynamics with ab initio accuracy to 100 million atoms with machine learning. In *SC20: International Conference for High Performance Computing, Networking, Storage and Analysis*, pages 1–14. IEEE, 2020.
- ¹⁰⁴ Denghui Lu, Wanrun Jiang, Yixiao Chen, Linfeng Zhang, Weile Jia, Han Wang, and Mohan Chen. Dp train, then dp compress: Model compression in deep potential molecular dynamics. *arXiv preprint arXiv:2107.02103*, 2021.
- ¹⁰⁵ Hao Wang, Xun Guo, Linfeng Zhang, Han Wang, and Jianming Xue. Deep learning interatomic potential model for accurate irradiation damage simulations. *Applied Physics Letters*, 114(24):244101, 2019.

Supplementary Material for
A Tungsten Deep Neural-Network Potential for Simulating
Mechanical Property Degradation Under Fusion Service
Environment

Xiaoyang Wang

*Laboratory of Computational Physics,
Institute of Applied Physics and Computational Mathematics,
Huayuan Road 6, Beijing, P. R. China*

Yinan Wang

*School of Mathematical Sciences, Peking University,
No.5 Yiheyuan Road Haidian District, Beijing, P.R.China 100871*

Linfeng Zhang and Fu-Zhi Dai

*DP Technology, Beijing, 100080 and
AI for Science Institute, Beijing, 100084*

Han Wang*

*Laboratory of Computational Physics,
Institute of Applied Physics and Computational Mathematics,
Fenghao East Road 2, Beijing 100094, P.R. China and
HEDPS, CAPT, College of Engineering,
Peking University, Beijing 100871, P.R. China*

arXiv:2111.04281v3 [cond-mat.mtrl-sci] 20 Apr 2022

I. THE DEEP POTENTIAL MODEL

The deep potential (DP) model assumes the total energy of a system, denoted by E , is the summation of the energy contributions of each atom in the system, denoted by E_i , i.e.,

$$E = \sum_{i=1}^N E_i \quad (1)$$

where N is the number of atoms in the system. In metallic materials systems, we assume the energy contribution E_i depends on the local environment of the atom. To model E_i , we define the local environment matrix \mathcal{R}_i of a central atom i being the collection of the relative positions of all its neighbors j within a given cutoff radius r_c . The j -th line of the environment matrix is made up by the relative position to the j -th neighbor, i.e.

$$\{\mathcal{R}_i\}_{j,\cdot} = s(r_{ij}) \times \left(\frac{x_{ij}}{r_{ij}}, \frac{y_{ij}}{r_{ij}}, \frac{z_{ij}}{r_{ij}} \right), \quad (2)$$

where $\mathbf{r}_{ij} = \mathbf{r}_j - \mathbf{r}_i$ with \mathbf{r}_i being the position of atom i , (x_{ij}, y_{ij}, z_{ij}) denotes the three Cartesian coordinates of the vector \mathbf{r}_{ij} , and $r_{ij} = |\mathbf{r}_{ij}|$ stands for the distance between the neighbor j and the central atom i . The term $s(r_{ij})$ in Eq. (2) is defined as $s(r_{ij}) = f_c(r_{ij})/r_{ij}$ with f_c being a switching function smoothly varies from 1 to 0 at the cutoff distance. One possible construction of the switching function is

$$f_c(r) = \begin{cases} 1 & r < r_{cs} \\ u^3(-6u^2 + 15u - 10) + 1 & r_{cs} \leq r < r_c, \quad u = \frac{r - r_{cs}}{r_c - r_{cs}} \\ 0 & r_c \leq r \end{cases} \quad (3)$$

By this definition, f_c smoothly decays from 1 to 0 in the range $r_{cs} \leq r \leq r_c$. It can be shown that the second order derivative of f_c is continuous. The matrix \mathcal{R}_i has N_m lines, where N_m is the maximal possible number of neighbors of any atom in the system. If the actual number of neighbors of atom i is smaller than N_m , the rest places of the environment matrix are filled by zeros.

In the DP models, the local environment matrix is first mapped onto a descriptor \mathcal{D} , which preserves rotation, translation and permutation symmetries, and then mapped onto E_i via a **fitting net** \mathcal{F} .

$$E_i = \mathcal{F}(\mathcal{D}(\mathcal{R}_i)) \quad (4)$$

In the following sections, we introduce in detail the construction of the descriptor and the fitting net.

II. DESCRIPTORS

In this section we will introduce two types of descriptors, the two-body embedding descriptor that considers the embedding of only distances between atoms, and the three-body embedding descriptor that considers the embedding of the inner product of the relative positions of any two neighbors. The two-body embedding descriptor was originally introduced in Ref.⁷ as the descriptor for the smooth edition of the Deep Potential. The three-body embedding descriptor is proposed by this work.

A. Two-body embedding descriptor

In the construction of the two-body embedding descriptor $\mathcal{D}_i^{(2)}$, we firstly introduce the *generalized environment matrix* $\tilde{\mathcal{R}}_i$. This matrix has the same number of lines as the environment matrix, but has one more column made up of $s(r_{ij})$. The j -th row of $\tilde{\mathcal{R}}_i$ is defined as

$$\{\tilde{\mathcal{R}}_i\}_{j,\cdot} = s(r_{ij}) \times \left(1, \frac{x_{ij}}{r_{ij}}, \frac{y_{ij}}{r_{ij}}, \frac{z_{ij}}{r_{ij}}\right) \quad (5)$$

Similar to the environment matrix \mathcal{R}_i , if the number of neighbors of i is smaller than N_m , the empty positions of the generalized environment matrix $\tilde{\mathcal{R}}_i$ are filled with zeros.

We then introduce the *two-body embedding matrix* $\mathcal{G}_i^{(2)}$ that involves the embedding of two-atom distances. The embedding matrix $\mathcal{G}_i^{(2)}$ has N_m lines and M_2 columns. The j -th line is defined as

$$(\mathcal{G}_i^{(2)})_{j,\cdot} = \left(G_1^{(2)}(s(r_{ij})), \dots, G_{M_2}^{(2)}(s(r_{ij}))\right), \quad (6)$$

where $G^{(2)}$, the *two-body embedding net*, being a full connected deep neural network, maps the scalar $s(r_{ij})$ onto M_2 outputs. The embedding net $G^{(2)}$ has $m + 1$ layers, and can be mathematically written as

$$G^{(2)}(x) = \mathcal{L}_m^e \circ \mathcal{L}_{m-1}^e \circ \dots \circ \mathcal{L}_1^e \circ \mathcal{L}_0^e(x), \quad (7)$$

where \circ denotes the function composition. The first hidden layer \mathcal{L}_0^e takes a scalar as input and outputs a vector of size s_0 . It is defined by

$$\mathcal{L}_0^e(x) = \tanh(x \cdot W_0^e + b_0^e), \quad (8)$$

where $W_0^e \in \mathbb{R}^{s_0}$ are the weights, represented by a vector of size s_0 , $b_0^e \in \mathbb{R}^{s_0}$ denote the biases and the activation function \tanh applies to the vector $x \cdot W_0^e + b_0^e$ in a component-wise way. Other hidden layers are expressed as

$$\mathcal{L}_k^e(x) = (x, x) + \tanh(x \cdot W_k^e + b_k^e), \quad 1 < k \leq m \quad (9)$$

where (x, x) denotes the concatenation of two input vectors x . The weights are $W_k^e \in \mathbb{R}^{s_{k-1} \times s_k}$, and the biases are $b_k^e \in \mathbb{R}^{s_k}$. We let the output size of the k -th hidden layer be twice of the input size, i.e. $s_k = 2s_{k-1}$. The output size of the final layer, s_m , is equal to M_2 , which is the same as the number of columns of the embedding matrix $\mathcal{G}_i^{(2)}$. The parameters in the embedding net, $\{W_k^e, b_k^e\}_{k=0}^m$ will be trained together with the fitting net in an end-to-end way. The training of the DP model will be explained in Sect. IV.

With the generalized environment and the two-body embedding matrices in hand, we are ready to construct the two-body embedding descriptor $\mathcal{D}_i^{(2)}$:

$$\mathcal{D}_i^{(2)} = \frac{1}{N_m^2} (\mathcal{G}_i^{(2),<})^T \tilde{\mathcal{R}}_i (\tilde{\mathcal{R}}_i)^T \mathcal{G}_i^{(2)}, \quad (10)$$

where the superscript T denotes the matrix transpose. The superscript $<$ on $\mathcal{G}_i^{(2),<}$ means that $\mathcal{G}_i^{(2),<}$ is a sub-matrix of $\mathcal{G}_i^{(2)}$, taking the first $M^<$ columns of the latter matrix. The descriptor $\mathcal{D}_i^{(2)}$ is a matrix of shape $M^< \times M_2$, and is reshaped in to a vector before it is passed to the fitting net. The construction of the two-body embedding descriptor $\mathcal{D}_i^{(2)}$ is schematically illustrated in Fig.S1.

B. Symmetries of the two-body embedding descriptor

The two-body embedding descriptor $\mathcal{D}_i^{(2)}$ preserves the translation symmetry, because all elements of the generalized environment and the embedding matrices are functions of relative positions between atom i and its neighbors.

The two-body embedding matrix $\mathcal{G}_i^{(2)}$ is invariant to rotation transform, because the input of the embedding net is the distance between i and its neighbors, which is invariant to rotation. The matrix $\tilde{\mathcal{R}}_i (\tilde{\mathcal{R}}_i)^T$ is over-complete, with the jk -th element defined by

$$\{\tilde{\mathcal{R}}_i (\tilde{\mathcal{R}}_i)^T\}_{jk} = s(r_{ij})s(r_{ik}) \times \left(1 + \frac{\mathbf{r}_{ij} \cdot \mathbf{r}_{ik}}{r_{ij}r_{ik}}\right). \quad (11)$$

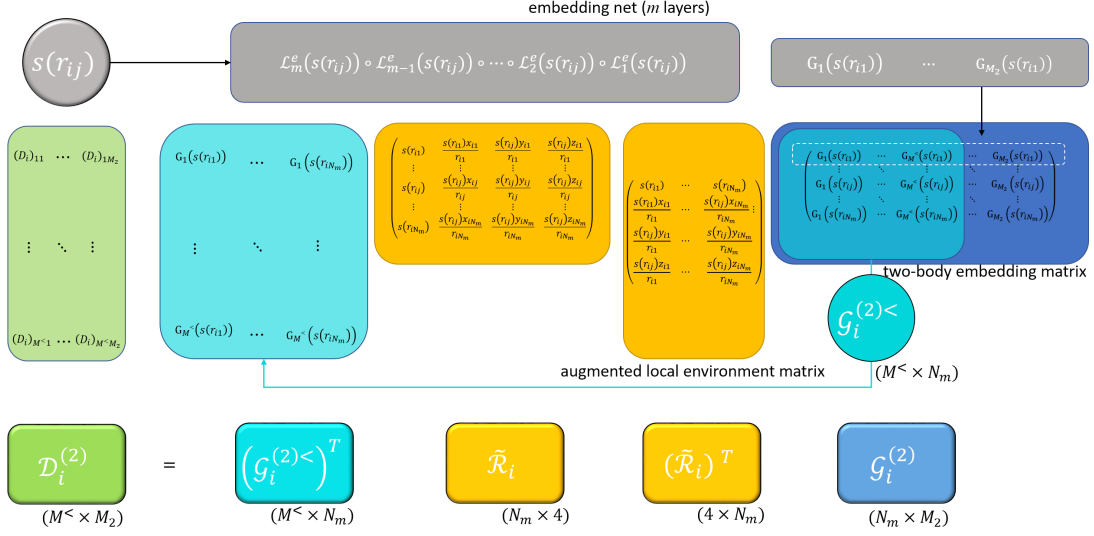


FIG. S1: Schematics of the two-body descriptor.

The jk -th element is invariant under rotational transform, because the inner product $\mathbf{r}_{ij} \cdot \mathbf{r}_{ik}$ and the distances r_{ij} , r_{ik} are invariant under rotation. Therefore the two-body embedding descriptor $\mathcal{D}_i^{(2)}$ preserves the rotational symmetry.

The $\alpha\beta$ -th element of the matrix product $(\tilde{\mathcal{R}}_i)^T \mathcal{G}_i^{(2)}$ is written as

$$\{(\tilde{\mathcal{R}}_i)^T \mathcal{G}_i^{(2)}\}_{\alpha,\beta} = \sum_{j=1}^{N_m} \{\tilde{\mathcal{R}}_i\}_{\alpha,j} \{\mathcal{G}_i^{(2)}\}_{j,\beta}, \quad (12)$$

where $\{\tilde{\mathcal{R}}_i\}_{\alpha j}$ and $\{\mathcal{G}_i^{(2)}\}_{j\beta}$ are the αj -th and $j\beta$ -th element of the generalized environment and the embedding matrices, respectively. The summation in Eq. (12) ensures that the product $(\tilde{\mathcal{R}}_i)^T \mathcal{G}_i^{(2)}$ is invariant under any change in the order of neighbors of the same chemical species, thus preserves the permutational symmetry. Similar argument applies to the product $(\mathcal{G}_i^{(2)<})^T \tilde{\mathcal{R}}_i$, thus the two-body embedding descriptor preserves the permutational symmetry.

C. Three-body embedding descriptor

The three-body embedding descriptor $\mathcal{D}_i^{(3)}$ is distinguished from the two-body embedding descriptor $\mathcal{D}^{(2)}$ by the embedding matrix. We firstly introduce a short-hand notation $(\theta_i)_{jk}$ for the elements of the product of the environment matrix with its transpose. By Eq. (2),

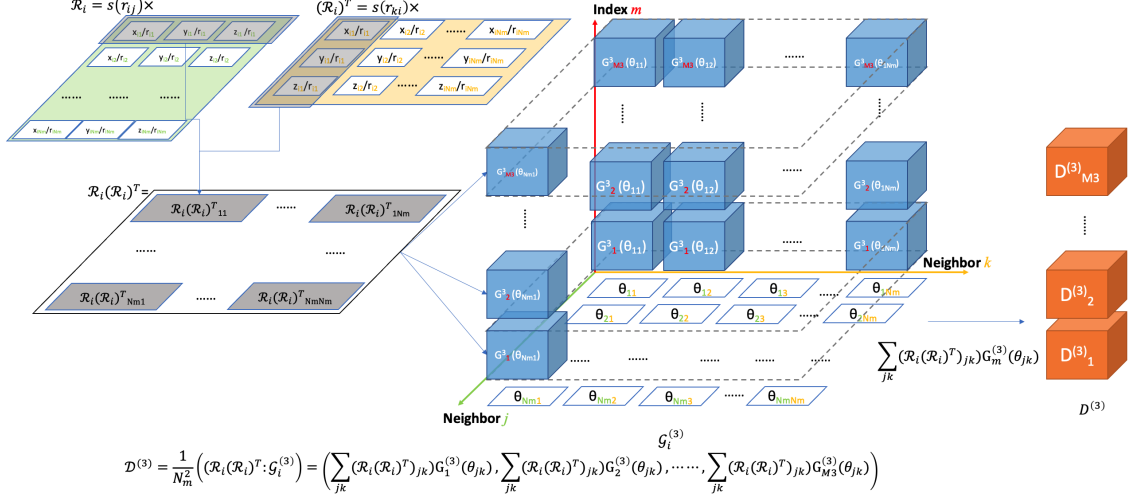


FIG. S2: Schematics of the three-body descriptor.

we have

$$(\theta_i)_{jk} \equiv \{\mathcal{R}_i(\mathcal{R}_j)^T\}_{jk} = s(r_{ij})s(r_{jk}) \frac{\mathbf{r}_{ij} \cdot \mathbf{r}_{ik}}{r_{ij}r_{ik}}. \quad (13)$$

For any atom i we define the three-body embedding tensor $\mathcal{G}_i^{(3)}$, which is an order-3 tensor, as

$$(\mathcal{G}_i^{(3)})_{jk,\cdot} = \left(G_1^{(3)}((\theta_i)_{jk}), \dots, G_{M_3}^{(3)}((\theta_i)_{jk}) \right), \quad (14)$$

where $G^{(3)}$, called the *three-body embedding net*, maps the scalar $(\theta_i)_{jk}$ to a vector of dimension M_3 . It is represented by a full connected feed forward deep neural network, which has the same architecture as the two-body embedding net defined by Eqs. (7)–(9). We denote the number of layers of the three-body embedding net by $m_t + 1$, and denote the trainable parameters of it by $\{W_k^t, b_k^t\}_{k=0}^{m_t}$. The first two indices, i.e. j and k , of the embedding tensor $\mathcal{G}_i^{(3)}$ go from 1 to N_m .

Based on the environment matrix and the three-body embedding matrix, we propose the following form of the three-body embedding descriptor $\mathcal{D}_i^{(3)}$

$$\mathcal{D}_i^{(3)} = \frac{1}{N_m^2} \theta_i : \mathcal{G}_i^{(3)} = \frac{1}{N_m^2} \sum_{jk=1}^{N_m} (\theta_i)_{jk} (\mathcal{G}_i^{(3)})_{jk}, \quad (15)$$

where $:$ denotes the double contraction operation. The construction of the three-body descriptor $\mathcal{D}_i^{(3)}$ is schematically explained in Fig.S2. It can be understood as multiplying each

element in $\mathcal{G}_i^{(3)}$ with the element having the same (j, k) subscript in the $N_m \times N_m$ matrix θ_i , then sum them all together as one element in $\mathcal{D}_i^{(3)}$. The descriptor is a vector of dimension M_3 .

D. Symmetries of the three-body embedding descriptor

The three body embedding descriptor is invariant under the translation of the positions of atoms, because the environment matrix \mathcal{R}_i is defined as a function of relative positions between atom i and its neighbors.

By Eq. (13), $(\theta_i)_{ij}$ is invariant with rotational transform, because we have dot product of \mathbf{r}_{ij} and \mathbf{r}_{ik} and their lengths on the right-hand-side of the definition, which are all invariant under rotation. This leads to the fact that the three-body embedding tensor $\mathcal{G}_i^{(3)}$, as a function of $(\theta_i)_{ij}$, is also invariant with rotational transforms. Thus the descriptor $\mathcal{D}_i^{(3)}$ preserves the rotational symmetry.

The summation over neighbor indices j and k in Eq. (15) ensures that the descriptor $\mathcal{D}_i^{(3)}$ is invariant with any change in the order of neighbors of the same chemical species, thus the permutational symmetry is preserved.

E. Hybridization of descriptors and the computational complexity

In our DP-HYB model, the descriptor is the hybridization of the two-body embedding descriptor $\mathcal{D}_i^{(2)}$ and our newly proposed three body embedding descriptor $\mathcal{D}_i^{(3)}$, i.e.

$$\mathcal{D}_i = (\mathcal{D}_i^{(2)}, \mathcal{D}_i^{(3)}), \quad (16)$$

where the notation (\cdot, \cdot) means that both descriptors $\mathcal{D}^{(2)}$ and $\mathcal{D}^{(3)}$ are treated as vectors, and the two vectors are concatenated to form a new vector. Thus the hybrid descriptor \mathcal{D}_i has a total number of $M^< \times M_2 + M_3$ outputs. The parameters needed to be determined in the training are $\{W_k^e, b_k^e\}_{k=0}^m, \{W_k^t, b_k^t\}_{k=0}^{m_t}$.

The computational cost of the environment \mathcal{R}_i and the two-body embedding $\mathcal{G}_i^{(2)}$ matrices are of order $\mathcal{O}(N_m)$. The cost of matrix multiplications in Eq. (10) is $\mathcal{O}(N_m)$. If we denote the number of atoms in the system by N , then the total computational cost of two-body descriptors of all atoms is $\mathcal{O}(N \times N_m)$, which is in proportion with the total number of

atoms N , and maximum number of neighbors N_m . The computational cost of the three-body embedding tensor $\mathcal{G}_i^{(3)}$ is $\mathcal{O}(N_m^2)$. The cost of the double contraction in Eq. (15) is also $\mathcal{O}(N_m^2)$. The computational cost of the three-body embedding descriptors of all atoms is $\mathcal{O}(N \times N_m^2)$. Considering the computational cost, the cut-off radius used to calculate the three-body embedding descriptor is usually chosen to be smaller than that used to calculate the two-body embedding descriptor.

III. FITTING NET

The fitting net maps the descriptor \mathcal{D}_i to the energy contribution E_i of each atom i . Fitting net is a fully connected deep neural network with skip-connections, and contains l hidden layers. It is written as

$$\mathcal{F}(x) = \mathcal{L}_l^f \circ \dots \circ \mathcal{L}_1^f \circ \mathcal{L}_0^f(x). \quad (17)$$

The layers of the fitting net are defined as

$$\mathcal{L}_0^f(x) = \tanh(x \cdot W_0^f + b_0^f) \quad (18)$$

$$\mathcal{L}_k^f(x) = x + \tanh(x \cdot W_k^f + b_k^f), \quad 1 \leq k < l \quad (19)$$

$$\mathcal{L}_l^f(x) = x \cdot W_l^f + b_l^f \quad (20)$$

In the first hidden layer \mathcal{L}_0^f , the weights W_0^f and bias b_0^f are of size $(M^< \times M_2 + M_3) \times M_F$ and M_F , respectively. In the layers $1 \leq k < l$, the input and output are vectors of the same length M_F , thus a skip connect is setup, see Eq. (19). The weights and biases are of size $M_F \times M_F$ and M_F , respectively. The output layer \mathcal{L}_l^f is a linear transform that maps vector of length M_F to a scalar. The weights W_l^f form a vector of size M_F , and the bias is a scalar. All the parameters $\{W_k^f, b_k^f\}_{k=0}^l$ are optimized together with the parameters in the descriptor during the training.

IV. TRAINING

In the DP model, the system energy is the summation of atomic energy contributions,

$$E = \sum_i E_i = \sum_i \mathcal{F}(\mathcal{D}_i) = \sum_i \mathcal{F}(\mathcal{D}(\mathcal{R}_i)). \quad (21)$$

Since the descriptor is a function of the environment matrix, we denote $\mathcal{D}_i = \mathcal{D}(\mathcal{R}_i)$. The forces F_i of an atom i can be calculated by

$$F_i = -\nabla_{r_i} E \quad (22)$$

The virial tensor of a system is defined as:

$$\Xi_{\alpha\beta} = -\frac{\partial E}{\partial h_{\gamma\alpha}} h_{\gamma\beta} \quad (23)$$

where $h_{\alpha\beta}$ is the β th component of α th basis vector of the simulation cell.

During the training processes, the weights and biases of the embedding nets ($\{W_k^e, b_k^e\}_{k=0}^m$, $\{W_k^t, b_k^t\}_{k=0}^{m_t}$) and those of the fitting net ($\{W_k^f, b_k^f\}_{k=0}^l$) are trained to minimize the loss function

$$\mathcal{L} = \frac{1}{|\mathcal{B}|} \sum_{k \in \mathcal{B}} \left(p_\epsilon \frac{1}{N} |\hat{E}^k - E^k|^2 + p_f \frac{1}{3N} \sum_{i\alpha} |\hat{F}_{i\alpha}^k - F_{i\alpha}^k|^2 + p_\xi \frac{1}{9N} \sum_{i\alpha} |\hat{\Xi}_{\alpha\beta}^k - \Xi_{\alpha\beta}^k|^2 \right), \quad (24)$$

which measures the difference between the DFT energy \hat{E}^k , forces $\hat{F}_{i\alpha}^k$ and the virial tensor $\hat{\Xi}_{\alpha\beta}^k$, and those predicted by the model. In this work, the Adam stochastic gradient descent optimizer² is used in the training. In Eq. (24), \mathcal{B} is a mini-batch of datasets, and $|\mathcal{B}|$ denotes the batch size. The superscript k denotes the index of the training data in the mini-batch. Each training datum contains the configuration of the system (including the coordinates of atoms, the box basis vectors and the element types), and the corresponding labels (total energy, forces on each atoms, and the virial tensor), which are obtained by a DFT calculation. Prefactors (p_ϵ, p_f, p_ξ) are a set of hyper-parameters determining the relative importance of the energy, forces and virial tensor during the training. The prefactors are gradually adjusted according to the learning rate $r_l(t)$, which exponentially decays with the training step t :

$$r_l(t) = r_l^0 k_d^{t/t_d}, \quad (25)$$

where r_l^0 is the learning rate at the beginning, t_d denotes the typical timescale of learning rate decaying and k_d denotes the decay rate. The prefactors vary with the learning rate in the following way

$$p_\alpha(t) = p_\alpha^{limit} \left[1 - \frac{r_l(t)}{r_l^0} \right] + p_\alpha^{start} \left[\frac{r_l(t)}{r_l^0} \right], \quad \alpha = \epsilon, f, \text{ or } \xi, \quad (26)$$

$p_\alpha(t)$ is either of the three pre-factors (p_ϵ, p_f, p_ξ) at training step t . p_α^{start} and p_α^{limit} are the pre-factors at the beginning and at an infinitely small learning rate. The prefactors change linearly from the p_α^{start} to p_α^{limit} during the training process. In practice, a relatively larger force prefactor at the beginning and balanced prefactors at the end of the training can make the best use of the training datasets and achieve relatively good accuracy.

V. HYPER-PARAMETERS

The training parameters used during the training step of the DP-GEN scheme and those used for training the productive DP models are summarized in Tab. S1.

* Electronic address: wang_han@iapcm.ac.cn

TABLE S1: Hyper-parameters used during the training in the DP-GEN iterations and the training of the productive models. The parameters used in the first and second refinements are listed in parenthesis respectively. The superscript (2) and (3) denotes the hyper-parameter used in two-body embedding descriptors $\mathcal{D}^{(2)}$ and three-body embedding descriptors $\mathcal{D}^{(3)}$, respectively.

Hyper-parameter	DP-GEN Iterations	Productive Model DP-SE2	Productive Model DP-HYB
$r_c^{(2)}$	6.0Å	6.0Å	6.0Å
$r_{cs}^{(2)}$	2.0Å	2.0Å	2.0Å
$N_m^{(2)}$	100	100	100
layers of $\mathcal{G}^{(2)}$	20,40,80	20,40,80	20,40,80
M_2	80	80	80
$M^<$	16	16	16
$r_c^{(3)}$	-	-	4.0Å
$r_{cs}^{(3)}$	-	-	2.0Å
$N_m^{(3)}$	-	-	32
layers of $\mathcal{G}^{(3)}$	-	-	4,8,16
M_3	-	-	16
M_F	240	240	240
r_l^0	0.001	0.001(0.0001,0.0001)	0.001(0.0001,0.0001)
k_d	0.95	0.95	0.95
t_d	2×10^3	$120 \times 10^3(5 \times 10^3, 20 \times 10^3)$	$120 \times 10^3(5 \times 10^3, 20 \times 10^3)$
p_ϵ^{start}	0.02	0.02(1.0, 1.0)	0.02(1.0, 1.0)
p_ϵ^{limit}	1.0	1.0(1.0, 1.0)	1.0(1.0, 1.0)
p_f^{start}	1000.0	1000.0(1.0, 1.0)	1000.0(1.0, 1.0)
p_f^{limit}	1.0	1.0(1.0, 1.0)	1.0(1.0, 1.0)
p_ξ^{start}	0.02	0.02(0.9, 0.9)	0.02(0.9, 0.9)
p_ξ^{limit}	1.0	1.0(1.0, 1.0)	1.0(1.0, 1.0)
Activation Function	tanh	tanh	tanh
Training Steps	0.4×10^6	$24 \times 10^6(1 \times 10^6, 4 \times 10^6)$	$24 \times 10^6(1 \times 10^6, 4 \times 10^6)$